JGR Atmospheres

RESEARCH ARTICLE
10.1029/2025JD044185

Sensitivity of the 2023 Asian Summer Monsoon Water Vapor Transport to Arabian Sea Surface Temperature Anomalies

Rui Sun[1], Aneesh C. Subramanian[2], Brandon O. Wolding[3,4], Tien-Yiao Hsu[1], Matthew R. Mazloff[1], Bruce D. Cornuelle[1], Janet Sprintall[1], Arthur J. Miller[1], Ganesh Gopalakrishnan[1], Prajeesh Ag[5,6], and Ibrahim Hoteit[5,6]

[1]Scripps Institution of Oceanography, La Jolla, CA, USA, [2]Department of Atmospheric and Oceanic Sciences, University of Colorado Boulder, Boulder, CO, USA, [3]Cooperative Institute for Research in Environmental Sciences, University of Colorado Boulder, Boulder, CO, USA, [4]NOAA Physical Sciences Laboratory, Boulder, CO, USA, [5]Physical Sciences and Engineering Division, King Abdullah University of Science and Technology (KAUST), Thuwal, Saudi Arabia, [6]Climate Change Center, National Center for Meteorology, Jeddah, Saudi Arabia

Key Points:

- If the SST declines more slowly than normal, the precipitation increases by more than 100% around the ASMWP, but decreases outside the ASMWP
- The IVT sensitivity analysis shows that water vapor and wind contribute to the precipitation changes
- From an idealized plume model, changes in humidity lead to most of the differences in atmospheric buoyancy that change the precipitation

Correspondence to:
R. Sun,
rus043@ucsd.edu

Citation:
Sun, R., Subramanian, A. C., Wolding, B. O., Hsu, T.-Y., Mazloff, M. R., Cornuelle, B. D., et al. (2026). Sensitivity of the 2023 Asian summer monsoon water vapor transport to Arabian Sea surface temperature anomalies. *Journal of Geophysical Research: Atmospheres*, *131*, e2025JD044185. https://doi.org/10.1029/2025JD044185

Received 24 APR 2025
Accepted 19 MAR 2026

Author Contributions:
Conceptualization: Aneesh C. Subramanian
Formal analysis: Rui Sun, Aneesh C. Subramanian, Tien-Yiao Hsu, Matthew R. Mazloff, Bruce D. Cornuelle, Janet Sprintall, Arthur J. Miller, Ganesh Gopalakrishnan, Prajeesh Ag, Ibrahim Hoteit
Funding acquisition: Aneesh C. Subramanian, Ibrahim Hoteit
Investigation: Rui Sun
Methodology: Brandon O. Wolding
Software: Rui Sun, Brandon O. Wolding
Supervision: Aneesh C. Subramanian, Matthew R. Mazloff, Bruce D. Cornuelle, Ibrahim Hoteit
Visualization: Rui Sun
Writing – original draft: Rui Sun
Writing – review & editing: Rui Sun, Aneesh C. Subramanian, Brandon O. Wolding, Tien-Yiao Hsu, Matthew R. Mazloff, Bruce D. Cornuelle, Janet Sprintall, Arthur J. Miller, Ganesh Gopalakrishnan, Prajeesh Ag, Ibrahim Hoteit

Abstract Prior to the onset of the South Asian monsoon, the Arabian Sea experiences a warming phase during which the Arabian Sea mini warm pool (ASMWP) becomes one of the world's warmest oceanic regions, characterized by sea surface temperatures (SSTs) exceeding 30°C. To understand the role of this warming in monsoon evolution, we performed an SST sensitivity experiment using the Weather Research and Forecasting (WRF) atmospheric model. Our case study focuses on the 2023 monsoon, which was characterized by high initial SST that declined faster than in normal years. We found that if the SST declines more slowly than normal, the off-shore precipitation increases by more than 100% around the ASMWP, but decreases in the northern Arabian Sea and the western coast of India. To understand the precipitation differences, we separated the components of the integrated vapor transport (IVT) and found that the changes in both water vapor and wind affect precipitation. The analysis revealed that the changes in water vapor are due to (a) stronger evaporation and precipitation in the ASMWP, and (b) moisture advection outside the ASMWP. It is also shown that the pressure adjustment mechanism can explain the changes in wind speed. With warmer SST conditions, the atmosphere pressure drops and causes wind convergence, thereby creating a weak cyclonic wind anomaly that redistributes the water vapor. Finally, we examined the vertically integrated buoyancy in the context of an idealized plume model. In the ASMWP, temperature changes contribute to increases in buoyancy below 850 hPa, but humidity changes contribute to far more increases in buoyancy between 800 and 600 hPa, which enhance the convection and lead to more precipitation.

Plain Language Summary Before the South Asian monsoon, the Arabian Sea mini warm pool (ASMWP) becomes one of the world's warmest oceanic regions. To understand the impact of the warm pool on the monsoon, we performed numerical simulations focusing on the 2023 monsoon when the ocean temperature was high and declined faster. Based on the simulations, we found that the precipitation increases by 100% in the warm pool if the ocean temperature declines more slowly, but the precipitation outside the warm pool decreases when the ocean gets warmer. To understand the precipitation differences, we analyzed the output from the numerical model and found that the changes in humidity and wind are important. Our analysis revealed that the changes in humidity are due to (a) stronger evaporation and precipitation in the warm pool, and (b) changes in wind speed outside the warm pool that redistribute the water vapor. The changes in wind speed are due to a weak cyclone generated by the ocean temperature differences in the mini warm pool. In the vertical direction, the humidity changes lead to the instabilities of the atmosphere that contribute to more precipitation.

1. Introduction

Understanding and predicting the Indian monsoon is essential for the well-being of over 1 billion people inhabiting the surrounding region (Gadgil, 2003). Before the onset of the South Asian monsoon, the Arabian Sea experiences a warming phase. During this period the Arabian Sea mini warm pool (ASMWP) becomes one of the world's warmest oceanic regions, characterized by sea surface temperatures (SSTs) exceeding 30°C (Kurian & Vinayachandran, 2007; Shenoi et al., 1999). Compounding this, a pronounced warming trend has been further reported over the past century in the ASMWP region (Nagamani et al., 2016) and the broader tropical Indian Ocean (Roxy et al., 2020).

Several studies have examined the connection between the monsoon and the ASMWP region. The early study of Washington et al. (1977) discussed the monsoon response to different SST conditions in the Arabian Sea. The most significant changes are increased vertical wind and precipitation over warm anomalies, and decreased vertical wind and precipitation in some regions adjacent to the region with prescribed SST changes. Chen and van Loon (1987) examined the interannual variation of monsoon jets due to SST changes. In addition, Rao and Sivakumar (1999) proposed a possible mechanism for the evolution of the warm pool. They hypothesized that the warm pool is formed when the radiative heat input overwhelms turbulent heat loss at the air–sea interface. They also found that on most occasions the onset vortex arises over the ASMWP region. Later, Vinayachandran et al. (2007) reported that the ASMWP is not sufficient to guarantee the generation of the monsoon onset vortex.

To further improve the understanding of the dissipation of the ASMWP and the Indian monsoon onset, Neema et al. (2012) investigated the thermal characteristics of the ASMWP using satellite observations, reanalysis products, and model simulations. Using the data from 1960 to 2010, they noticed that the ASMWP reaches its maximum SST 2 weeks prior to the monsoon onset, and then began to dissipate after the monsoon onset took place. In many cases, larger and warmer ASMWPs are associated with stronger monsoon years, whereas smaller and cooler ASMWPs are associated with weaker monsoons. In addition, Roman-Stork et al. (2020) examined the role of freshwater transport from the Bay of Bengal into the southeastern Arabian Sea which encompasses the ASMWP. Satellite-derived data and reanalysis products were used to study the variability of ocean heat content, atmospheric moisture flux, and mixed layer depth. In their analysis, low-salinity water has a significant impact on barrier layer formation in the southeastern Arabian Sea and the vertical structure of the ASMWP. The long-term decadal variations in atmospheric moisture flux, freshwater transport, and ocean heat content contributed to a lack of strong monsoons in recent years. Recently, Li et al. (2023) investigated the intraseasonal and interannual variability of SST in the ASMWP region. They found that when an El Niño (La Niña) event peaked in the winter of the previous year, the warm pool before the monsoon was more significant (insignificant) in the following year.

There have been various studies on the ASMWP relationship to long-term variability of monsoon intensity. However, there has yet to be a focused study on the impact of ASMWP intensity on monsoon precipitation at seasonal to subseasonal time scale. In addition, although precipitation events are associated with the water vapor transport of the monsoon (e.g., Lakshmi et al., 2019), there are no studies focusing on the direct response of water vapor transport to ASMWP variability. In this context, we conduct an experiment to investigate the effect of the ASMWP on the Indian summer monsoon using the Weather Research and Forecasting (WRF) model. To understand the role of ASMWP in precipitation and water vapor transport, a sensitivity analysis is performed by comparing two WRF simulations with different sea surface temperature (SST) forcings. We selected the 2023 monsoon season because the ASMWP starts with warmer SST and cools down much faster than in other years, which allows us to study the sensitivity of monsoon precipitation and water vapor transport to ASMWP changes. The present work is also inspired by the "Enhancing Knowledge of the Arabian Sea Marine Environment through Science and Advanced Training (EKAMSAT)" program for the 2023 monsoon season to understand the processes leading to moisture and precipitation biases in the monsoon forecasts. In this case study, we find that when SST cools more slowly than usual, the simulation results suggest that offshore precipitation in the warm pool increases, while precipitation outside the warm pool decreases. To understand the changes in water vapor transport, which is important for the prediction of precipitation, we analyze the integrated vapor transport (IVT, Lavers et al., 2016; Ralph et al., 2019) and find similar changes in IVT as found for precipitation. We then evaluate the contribution of the wind and water vapor changes to the IVT differences. In addition to the horizontal water vapor transport, we examine the vertical convection and stability of the atmosphere based on an idealized plume model (Wolding et al., 2024) to further evaluate the changes in precipitation. Although it is likely to be important, the feedback of the ocean to the atmosphere (other than via SST) is not investigated in this case study and will be explored in future work.

The manuscript is organized as follows. We first introduce the experimental setup and validation data in Section 2. The differences between the precipitation and water vapor transport resulting from the SST sensitivity experiments are presented in Section 3. Section 4 discusses the IVT differences between the two sensitivity experiments. Section 5 demonstrates the differences in thermodynamic stratification and convective instability. The final Section 6 outlines the main findings and conclusions.

2. Experimental Design

2.1. SST Sensitivity Experiment

To study the sensitivity of early monsoon stages to SST perturbations, we use version 4.5.2 of the WRF model (Skamarock et al., 2019) and perform simulations for the period from 01 June to 01 August 2023. The model domain extends from 5.24°S to 30.6°N and from 30°E to 91.44°E to cover the Arabian Sea, the Red Sea, and the Arabian Gulf. The horizontal grid has 768 × 448 cells (latitude × longitude) with 0.08° grid spacing. There are 40 sigma layers in the vertical direction (top pressure is 50 hPa). Two WRF experiments were performed, each with different SST forcings:

1. *ATM.control* uses the SST from the Met Office's Operational Sea Surface Temperature and Ice Analysis system (OSTIA, Donlon et al., 2012).
2. *ATM.warmer* adds a warmer SST perturbation to OSTIA analysis in the ASMWP region. This experiment aims to highlight the impact of the warm pool on the monsoon.

The SST perturbation is based on the initial SST condition in the warm pool region:

$$\mathrm{SST}_{p,n} = \alpha \mathrm{SST}_0 + (1-\alpha)\mathrm{SST}_n, \tag{1}$$

where SST_0 and SST_n are the OSTIA SST at the simulation start time and time step n, respectively; $\mathrm{SST}_{p,n}$ indicates the perturbed warmer SST at time step n; α is a 2-D Gaussian kernel function that limits the SST perturbation to the warm pool region:

$$\alpha = \exp\left(-\frac{(x-x_c)^2}{2\sigma_x^2} - \frac{(y-y_c)^2}{2\sigma_y^2}\right), \tag{2}$$

where $\exp(\cdot)$ is the exponential function; x and y are the longitude and latitude; $x_c = 68$ and $y_c = 12$ are the center of the Gaussian kernel at 68°E and 12°N; $\sigma_x = 6$ and $\sigma_y = 4$ are the zonal and meridional scales in degrees. In addition, when the initial SST_0 is cooler than SST_n, α is set to zero to avoid negative SST perturbations in the ATM.warmer case. It is noted at the center of the Gaussian kernel, the SST is persistent throughout the WRF simulation.

Figure 1 shows the SSTs in the two experiments and their differences, showing that the SST perturbation is largest near the center of the Gaussian kernel and smaller outside the warm pool region. To show the temporal evolution of the perturbed SST, we compare it with the OISST data from 1982 to 2023 (Huang et al., 2021; Reynolds et al., 2007). The SST is averaged between 6°–18°N ($x_c \pm 1.5\sigma_x$) and 59°–77°E ($y_c \pm 1.5\sigma_y$). The SST on 01 June 2023 is warmer than the 1981–2023 mean by about 1.5°, but Figure 1e shows that it cools down by about 1.5°C per month, which is faster than the 1981–2023 mean by about one standard deviation. To evaluate the sensitivity of the monsoon precipitation to the SST changes, we perturb the SST by one standard deviation of the historical SST data. Since the SST cools faster than the historical mean by one standard deviation, our perturbed experiment ATM.warmer cools at approximately the historical mean rate. Because the initial SST is warmer than the historical mean on 01 June, the SST throughout ATM.warmer is also warmer. By comparing the rate of SST changes in Figure 1e, the two experiments can shed light on the impact of the warm pool on the monsoon precipitation when the SST cools down faster or more slowly than average. The strong SST cooling during the first 3 weeks in the simulations is because of the passage of Cyclone Biparjoy between 06 June and 19 June. This motivated us to understand the sensitivity of the monsoon precipitation and water vapor transport under strong SST cooling conditions. We have also performed an additional experiment using 50% of the SST perturbation magnitude added in ATM. warmer, and found the IVT and precipitation responses are reduced by about 50% compared with ATM.control, indicating the conclusions drawn from our experiments are robust to the SST perturbation.

Except for the SST forcing, the identical initial and boundary conditions are used in the two experiments. The WRF models are initialized using ERA5 (ECMWF, 2017; Hersbach et al., 2023a, Hersbach et al., 2023b). The linearly interpolated 6-hourly ERA5 fields are used as the lateral boundary conditions for air temperature, wind speed, and humidity. The "specified" zone in WRF prescribes the lateral boundary values, and the "relaxation"

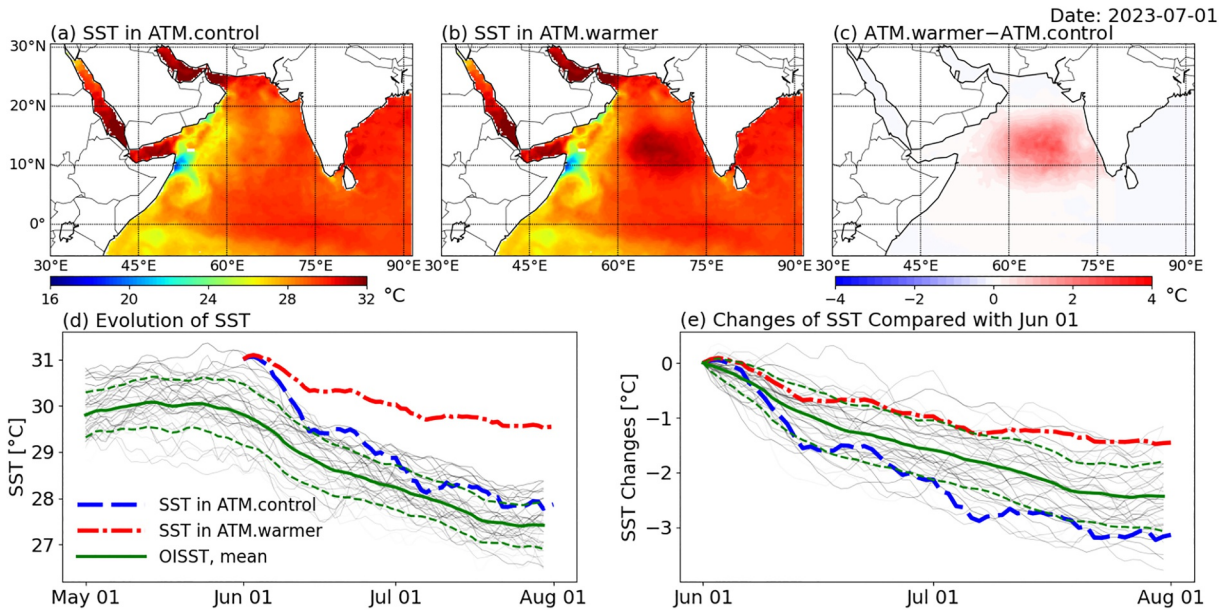

Figure 1. The SSTs used in the experiments to drive the WRF simulations. Panels (a, b) are the snapshots of SST on 01 July (1 month after the simulation start time) for ATM.control and ATM.warmer, respectively; Panel (c) is the SST difference between the snapshots (ATM.warmer−ATM.control); Panels (d, e), respectively, are the regional averaged SST evolution and the SST changes between 6°–18°N ($x_c \pm 1.5\sigma_x$) and 59°–77°E ($y_c \pm 1.5\sigma_y$). In Panels (d) and (e), the thick lines are the averaged SST from OISST (green), ATM.control (blue) and ATM.warmer (red); the dashed green lines are the 1981 to 2023 averaged OISST plus or minus one standard deviation; the solid thin lines in the background are the OISST evolution from each year between 1981 and 2023.

zone is used to nudge the solution from the domain interior toward the boundary condition value. We use the default width of one grid point for the specified zone and four grid points for the relaxation zone. Spectral nudging is applied to temperature, geopotential height, and wind above the planetary boundary layer (PBL) to reduce model bias compared to ERA5. It is demonstrated that spectral nudging can significantly improve the simulations in many applications (Bowden et al., 2012; Glisan et al., 2013; Radu et al., 2008; Tang et al., 2017) and Indian Ocean monsoon precipitation (Saikrishna et al., 2022). The wavelengths we used for spectral nudging are 300 km in both zonal and meridional directions, and thus only the larger-scale synoptic conditions are nudged. The nudging coefficients for all three variables discussed above are set to WRF default values of 0.0003. Because spectral nudging reduces the model's internal variability (Weisse et al., 2000), it allows us to compare the precipitation and water vapor transport in two WRF experiments without running a large ensemble of simulations. We have also validated the IVT obtained from the simulations, shown in Appendix A, and found that the simulation results are generally consistent with ERA5 after nudging.

The selection of WRF physics options for both experiments is based on our previous simulations for the Arabian Sea region (Sun et al., 2023). The Morrison 2-moment scheme (Morrison et al., 2009) is used to resolve the microphysics; the updated version of the Kain–Fritsch convection scheme (Kain, 2004) is used for cumulus parameterization; the Mellor–Yamada–Nakanishi–Niino 2.5-order closure scheme (Nakanishi & Niino, 2004, 2009) is used for the PBL and the surface layer; the Rapid Radiation Transfer Model for GCMs (RRTMG, Iacono et al., 2008) is used for longwave and shortwave radiation transfer through the atmosphere. Although the land temperature plays an important role in the monsoon processes (Meehl, 1994), in our work we only focus on the role of ocean SST in the ASMWP region. In both WRF experiments, the Noah land surface model (Tewari et al., 2004) is used for the land surface processes with the same settings.

2.2. Diagnosing Water Vapor Transport

We evaluate the integrated water vapor (IWV) and integrated vapor transport (IVT) during the 2023 monsoon. IWV is calculated from specific humidity q (kg/kg) in the atmosphere:

$$\mathrm{IWV} = \frac{1}{g}\int q\, dp, \tag{3}$$

where g is the gravitational acceleration (equal to 9.81 m/s^2) and p is pressure (Pa). IVT is calculated from specific humidity and wind speed:

$$\mathbf{IVT} = \frac{1}{g}\int q\mathbf{U}\, dp, \tag{4}$$

where $\mathbf{U}$ is the vector of horizontal wind speed. The IWV and IVT are integrated from the surface pressure p_{surface} to 300 hPa (Lavers et al., 2016; Sun et al., 2021). There are about 26 WRF sigma layers within this pressure range in the Arabian Sea region. Because the WRF pressure levels are the sum of the base pressure and perturbation pressure, the number of sigma layers is not persistent throughout the experiment when computing the IWV and IVT. To better illustrate the difference between model outputs, IWV and IVT are daily averaged (starting and ending at 0000 UTC) using hourly instantaneous diagnostics.

To understand the IVT differences obtained in the simulations, we decompose the IVT into the contributions from water vapor and wind speed. The difference in the IVT magnitude between the two simulations is:

$$\text{IVT}_{\text{diff}} = |\mathbf{IVT}_1| - |\mathbf{IVT}_2|. \tag{5}$$

Because IVT is a vector, the vector form of IVT difference can be decomposed as:

$$\Delta\mathbf{IVT} = \int \frac{1}{g}\left(q_1\boldsymbol{U}_1 - q_2\boldsymbol{U}_2\right)\mathrm{d}p \tag{6}$$

$$= \int \frac{1}{g}\left[q_1\left(\boldsymbol{U}_1 - \boldsymbol{U}_2\right) + \boldsymbol{U}_1\left(q_1 - q_2\right) - \left(q_1 - q_2\right)\left(\boldsymbol{U}_1 - \boldsymbol{U}_2\right)\right]\mathrm{d}p \tag{7}$$

$$= \int \frac{1}{g}\left(q_1\Delta\boldsymbol{U} + \boldsymbol{U}_1\Delta q\right)\mathrm{d}p + \text{residual}, \tag{8}$$

where Δ indicates the difference between two simulations; $q\Delta\boldsymbol{U}$ and $\boldsymbol{U}\Delta q$ denote the contributions from wind and water vapor differences, respectively; the residual term is of second order. Note that the differences are computed based on the diagnostic variables saved with respect to WRF model sigma layers and those terms are different between the two experiments, and thus there are numerical errors due to integration and interpolation. It is noted that all the right-hand side terms ($q\Delta\boldsymbol{U}$, $\boldsymbol{U}\Delta q$, and residual) in Equation 8 are vectors. To assess whether $q\Delta\boldsymbol{U}$ and $\boldsymbol{U}\Delta q$ terms increase or decrease the IVT, we calculate their projections on the IVT vector, which are defined as:

$$\Delta\text{IVT}_{\text{U}} = \int \frac{q\Delta\boldsymbol{U}}{g}\cdot\frac{\mathbf{IVT}}{|\mathbf{IVT}|}\, dp; \tag{9}$$

$$\Delta\text{IVT}_{\text{q}} = \int \frac{\boldsymbol{U}\Delta q}{g}\cdot\frac{\mathbf{IVT}}{|\mathbf{IVT}|}\, dp. \tag{10}$$

To further diagnose the changes in water vapor transport, we examine the individual components that contribute to the changes in IWV. The IWV tendencies (Guan et al., 2020; Seager & Henderson, 2013) are contributed from the convergence of IVT, evaporation (E), and precipitation (P):

$$\frac{1}{g}\frac{\partial}{\partial t}\int q\, dp = -\nabla\cdot\mathbf{IVT} + \text{E} - \text{P}. \tag{11}$$

If we decompose the convergence of IVT, we have:

$$\frac{1}{g}\frac{\partial}{\partial t}\int q\, dp = -\frac{1}{g}\int \mathbf{U}\cdot\nabla q\, dp - \frac{1}{g}\int q\nabla\cdot\mathbf{U}\, dp - \frac{1}{g}q_s\mathbf{U}_{\mathbf{s}}\cdot\nabla p_s + \text{E} - \text{P}, \tag{12}$$

where $\mathbf{U} \cdot \nabla q$ is the contribution from moisture advection; $q\nabla \cdot \mathbf{U}$ is the contribution from mass convergence; $q_s \mathbf{U_s} \cdot \nabla p_s$ is a surface term that increases IWV when wind blows down the surface pressure gradient (Guan et al., 2020; Seager & Henderson, 2013). Similar to IWV and IVT, these terms are computed as daily averages using hourly instantaneous diagnostics. The residual term from WRF outputs is not negligible (Fita et al., 2019; Guan et al., 2020), but it is not practical or feasible to output these terms at each time step. Some of the residual may be because the simulation results are nudged to an analysis. However, we can still compare the differences in advection, evaporation, and precipitation, which are the dominant terms governing water vapor transport (Guan et al., 2020).

2.3. Vertically Integrated Buoyancy

In addition to the horizontal motion of water vapor transport, this study also aims to understand the vertical motions of the water vapor in the ASMWP region. Under different SST conditions, we analyze the vertical distribution of water vapor, especially for those related to the heat and moisture transferred from the surface to the atmosphere. We analyze the lower-tropospheric convective instability to evaluate the vertical motion of the water vapor. To diagnose the changes in convective instability, we employed a "deep-inflow" entrainment profile, which prescribes mixing over a deep layer of the lower troposphere, and is supported by observational, modeling, and theoretical studies (Kingsmill & Houze Jr, 1999; Kuo & Neelin, 2022; McGee & van den Heever, 2014; Schiro et al., 2018). Mixing is prescribed to be largest near the surface and decreasing with height to a value of zero at 450 hPa, known as deep-inflow B (DIB, see Section 3a of Wolding et al. (2024) for details). Ice-liquid water potential temperature is conserved during phase change, and liquid water exceeding 1 g/kg is rained out (Bryan & Fritsch, 2004). The vertically integrated buoyancy $\langle B \rangle$ is computed as:

$$\langle B \rangle = \int_{p_{\text{surface}}}^{600\text{hPa}} R_d \left(T_{v,\text{plume}} - T_{v,\text{env}}\right) d\ln p, \tag{13}$$

where R_d is the ideal gas constant; $T_{v,\text{plume}}$ and $T_{v,\text{env}}$ are the virtual temperature of the plume and environment respectively. When using the integrated measure of buoyancy defined in Equation 13, the subscript $_{\text{DIB}}$ is used to indicate the computation of $\langle B \rangle$ using a DIB entrainment profile stability of the atmosphere. It is noted that the surface pressure can be smaller than 1,000 hPa in the WRF model, and thus we compute the $\langle B \rangle_{\text{DIB}}$ from p_{surface} instead. More details of the idealized plume model can be found in Appendix B and Wolding et al. (2024). We have demonstrated that the $\langle B \rangle_{\text{DIB}}$ computed from the WRF are consistent with the validation data, also shown in Appendix B.

3. Comparison Between the Simulations

3.1. Precipitation and Water Vapor Transport

The precipitation on 01 July 2023 from the two simulations under different SST conditions are presented in Figure 2. Although precipitation is daily averaged from hourly diagnostics, spatial variability is still pronounced in the simulated precipitation in north India, east Africa, Bay of Bengal, and the tropical Indian Ocean. In the ATM.warmer case, precipitation is higher in the warm pool region off-shore, but lower in the north Arabian Sea and the western coast of India. In the WRF simulations, heavy precipitation is also observed in the frontal region near the center of the IVT contour near 60°E. This phenomenon has been studied extensively for the atmospheric rivers (Ralph et al., 2018). It can be seen in the figure that the precipitation inside the warm pool increases coherently in ATM.warmer, but outside of the warm pool the precipitation differences are smaller scale and due to the internal variabilities of the atmosphere. To illustrate the influence of the warm pool SST throughout the event, the evolution of precipitation at two representative locations is presented in Figures 2d and 2e. We select the locations based on the coarse resolution grid that we used to compute the budget terms in Section 4.2. The south (north) one is the 14th grid in the zonal direction, and 8th (11th) grid in the meridional direction. Heavy rainfall is observed between 09 and 16 June due to Cyclone Biparjoy. After 16 June, the persistent monsoon rains can be seen in the warm pool (e.g., at 65.84°E, 15.24°N), and ATM.warmer shows more rain than ATM.control by 50–100 mm/day. There is less rain outside the warm pool (e.g., at 65.84°E, 22.92°N), and the precipitation rate in ATM.warmer is lower than ATM.control. The precipitation is shown on 01 July 2023 to highlight the daily precipitation differences. Other snapshots of precipitation are shown in Appendix C and show similar increases

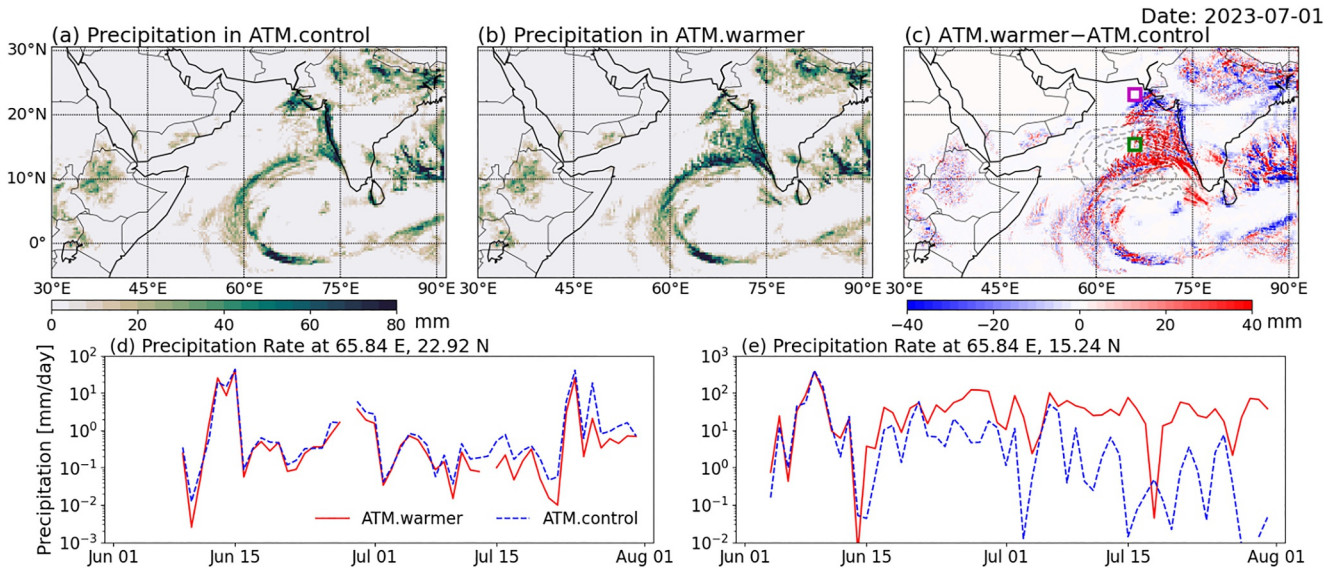

Figure 2. Daily precipitation obtained in the WRF simulations. Panels (a, b) are the daily average snapshots of precipitation from hourly diagnostics on 01 July obtained in ATM.warmer and ATM.control, respectively; Panel (c) is the difference between the two experiments (ATM.warmer−ATM.control); Panels (d, e) illustrate the evolution of precipitation at two representative locations (magenta box: 65.84°E, 22.92°N; green box: 65.84°E, 15.24°N) highlighted in Panel (c). The precipitation is averaged to a 0.32° resolution grid (every 4 grid points in the model). Note that the *y*-axes in (d, e) use a logarithmic scale, and thus no values are shown if there is no precipitation. The dashed contours in Panel (c) indicate the SST difference shown in Figure 1 at every 0.5°C.

and decreases for other dates. Although the Cyclone Biparjoy may lead to larger precipitation, because the activity of the cyclone is close to the simulation start time, there are much smaller precipitation differences before the landfall on 16 June than after.

We examine IVT changes in our simulations as they are associated with precipitation changes (Lakshmi et al., 2019; Raghuvanshi & Agarwal, 2023). The IVT is also dynamically connected with the extreme precipitation in the regions affected by Indian monsoon (Gimeno-Sotelo & Gimeno, 2023). The snapshots of the IVT and IVT differences are presented in Figure 3, again for 01 July 2023. As an important metric in predicting precipitation (Lavers et al., 2016; Ralph et al., 2019), IVT shows that the monsoon jet carries a significant amount of water to the east. The intensity and direction are slightly different in the two experiments: the IVT differences in Figure 3c suggest that ATM.warmer has increased IVT in the offshore region between 10 and 18°N, but decreased IVT in the north Arabian Sea, the western coast of India, and east of 75°E. The higher SST in the warm pool redistributes the water vapor not only in the warm pool region, but also affects the adjacent regions. In addition, the IVT evolution is presented in Figures 3d and 3e at the same locations as Figure 2. The IVTs are closer in the first 2 weeks when the SST difference is small (see Figure 1), but the differences are larger from the third week to the end of the simulation. In the warm pool (e.g., at 65.84°E, 15.24°N), IVT in ATM.warmer is persistently higher by about 100 kg/m/s (about 10%–15% of the total IVT throughout the simulation) after 01 July; outside the warm pool (e.g., at 65.84°E, 22.92°N), IVT in ATM.warmer is lower by about 20 kg/m/s. Compared with the precipitation differences in Figure 2c, the IVT differences inside and outside the warm pool are generally consistent, except for the regions with little rainfall. From the literature (Raghuvanshi & Agarwal, 2023), the correlation between the IVT and precipitation is more than 0.7 for the western coast of India. The IVT contours are also smoother and more predictive (Lavers et al., 2016) than precipitation for us to analyze the contribution of warmer SST, which motivates us to examine the IVT differences in the latter sections.

The evaporation rate, an important factor in determining the trend of water vapor, is approximately double for the ASMWP region between 10 and 18°N for ATM.warmer than ATM.control, from the third week to the end of simulation (Figure 4). The differences in the evaporation rate for the ASMWP region is due to the changes in SST in two WRF experiments. On the other hand, outside the warm pool region, the evaporation rate decreases slightly in the northern Arabian Sea. The decrease in evaporation is due to the changes in wind speed, which will be shown and discussed in the following section.

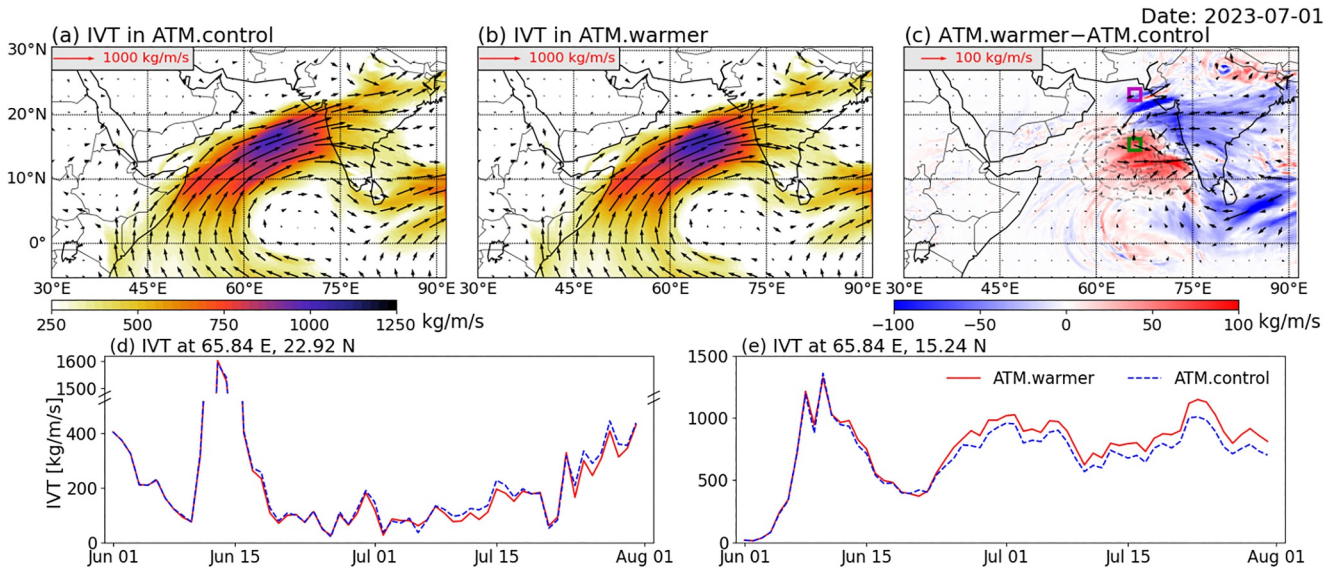

Figure 3. Daily averaged IVT obtained in the WRF simulations. Panels (a, b) are the snapshots of IVT (shading shows the magnitude and arrows show the direction) on 01 July obtained in ATM.control and ATM.warmer, respectively; Panel (c) is the difference between the two experiments (ATM.warmer−ATM.control); Panels (d, e) illustrate the evolution of IVT at two representative locations (magenta: 65.84°E, 22.92°N; green: 65.84°E, 15.24°N) highlighted in Panel (c). The dashed contours in Panel (c) indicate the SST difference shown in Figure 1 at every 0.5°(c).

3.2. Wind Speed and Sea Level Pressure

To understand the impact of the warm pool on the surface atmosphere, the 10-m wind speed and sea level pressure under different SST conditions are presented in Figure 5. The direction of the 10-m wind speed is close to the direction of IVT shown in Figure 3, indicating that lower-level wind contributes significantly to the water vapor transport. The wind speed difference is presented in Figure 5c, showing a cyclonic anomaly of the surface wind. The weaker surface wind speed in the northeast Arabian Sea may contribute to the decreased IVT and evaporation rate for that region; the stronger wind speed in the warm pool region is consistent with higher IVT and evaporation

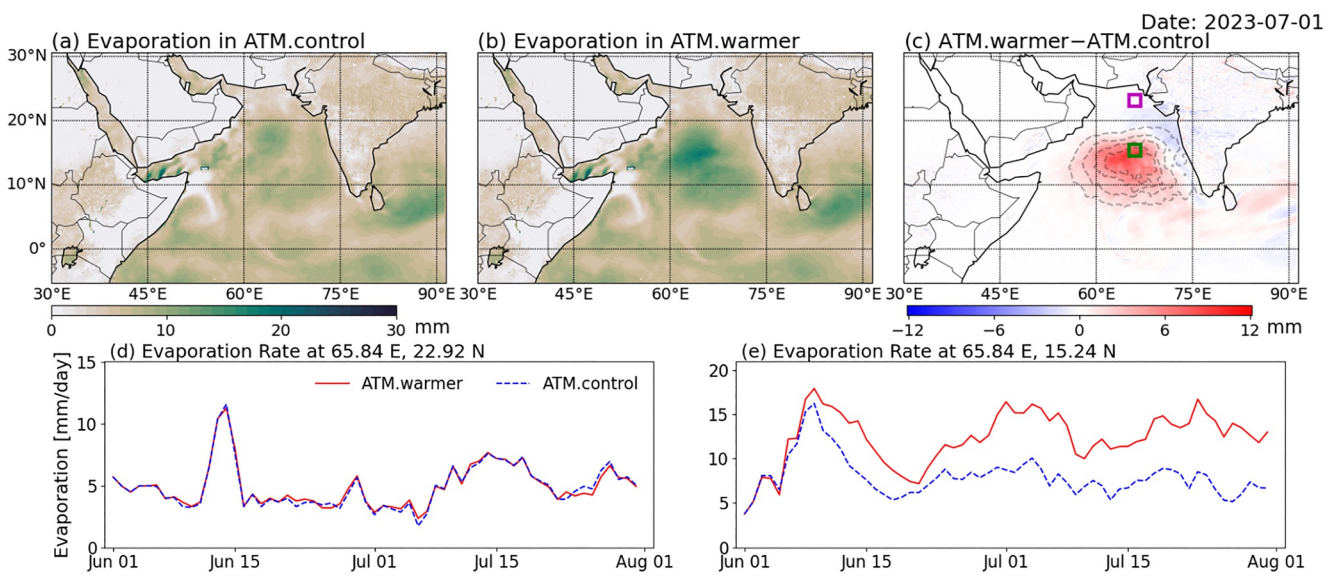

Figure 4. Daily evaporation obtained in the WRF simulations. Panels (a, b) are the snapshots of evaporation rate on 01 July obtained in ATM.control and ATM.warmer, respectively; Panel (c) is the difference between the two experiments (ATM.warmer−ATM.control); Panels (d, e) illustrate the evolution of evaporation rate at two representative locations (magenta: 65.84°E, 22.92°N; green: 65.84°E, 15.24°N) highlighted in Panel (c). The dashed contours in Panel (c) indicate the SST difference shown in Figure 1 at every 0.5°C.

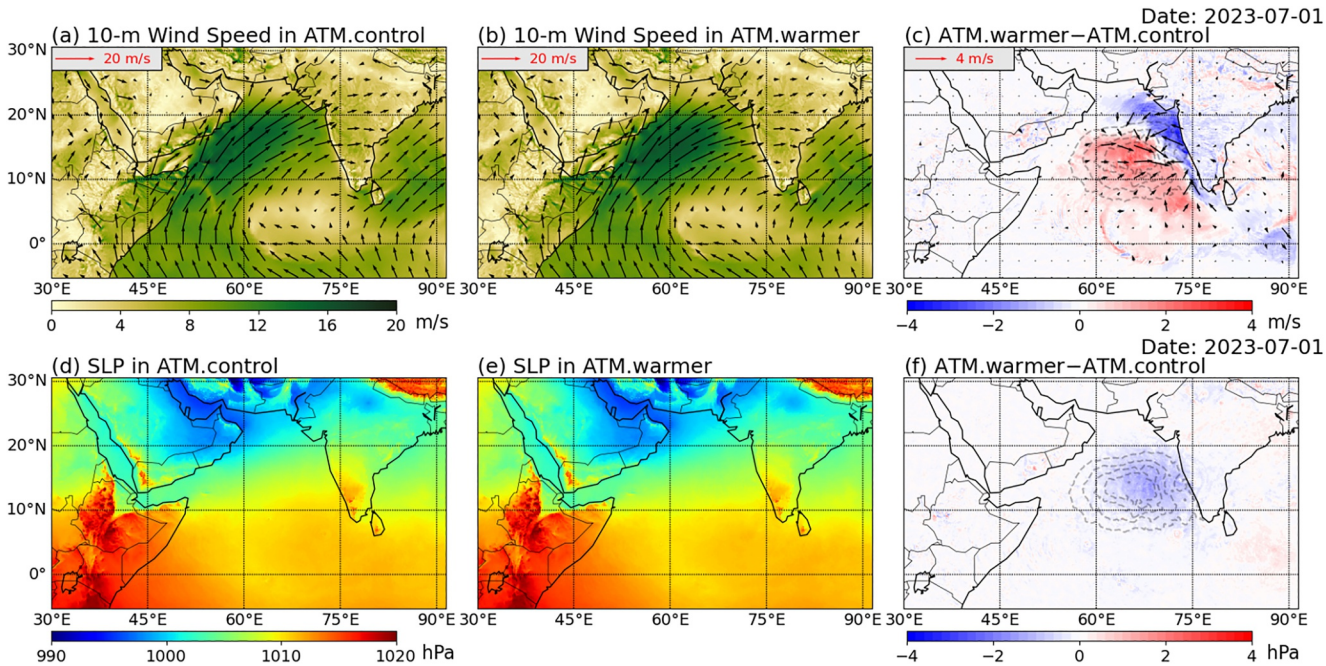

Figure 5. Comparison of 10-m wind speed (a, b) and sea-level pressure (d, e) and their difference (c, f) obtained from the experiments. In Panel (a, b), the shading shows the magnitude and arrows show the direction. The dashed contours in Panel (c, f) indicate the SST difference shown in Figure 1. The comparisons are shown for 01 July (1 month after the simulation start time).

rates. In addition, higher-level jets from the Arabian Peninsula play an important role in water vapor transport. However, their contributions are smaller than the lower-level winds (see further discussion in Appendix D).

During the monsoon season, the surface pressure is lower in the north Arabian Sea and higher in the south, shown in Figures 5d and 5e. The direction of wind speed follows the contours of the difference of SST and sea-level pressure. Due to warmer SST conditions in ATM.warmer, the pressure drops by about 2 hPa in the warm pool region. The changes in wind speed and pressure gradients can be explained using the pressure adjustment mechanism (Back & Bretherton, 2009; Lindzen & Nigam, 1987; Li & Carbone, 2012). The co-location of the warm pool and the low pressure gradients indicates that warmer SST affects air density and pressure. When there are horizontal temperature differences on the sea surface, the air above these varying temperatures will also have different temperatures. This thermal variation directly influences the atmospheric pressure, with warmer areas leading to lower pressure and cooler areas leading to higher pressure. These temperature-induced pressure gradients, in turn, force low-level atmospheric flow. Computed from the surface pressure gradient, the geostrophic wind magnitude and pattern (shown in Appendix D) are comparable to the wind speed differences shown in Figure 5c, indicating that the pressure adjustment mechanism explains the changes in wind speed. Surface ageostrophic winds are significant, however, leading to discrepancies between changes in geostrophic and total winds. We also find wind convergence (not shown) and secondary circulations generated due to the warmer SST, and the vertical wind speed increases by about 0.2 m/s. The secondary circulation in and around the warm pool region and the geostrophic wind speed are detailed in Appendix D.

3.3. Stability of Atmosphere

The warmer SST in ATM.warmer also changes the atmosphere's stability. To illustrate this, we use the PBL height and the vertically integrated buoyancy $\langle B \rangle_{\mathrm{DIB}}$ described in Section 2.3. Again, we use the snapshots on 01 July to illustrate the differences between the simulations. Figure 6 shows that PBL height is about 1,000 m in the ASMWP region in the two experiments. Under warmer SST conditions, the PBL height increases by about 200 m. This is because SST warms the surface air and makes the atmospheric boundary layer more unstable in ATM. warmer. It can also be seen in Figure 6 that the PBL height is low over the Red Sea and the Arabian Gulf (less than 400 m), suggesting a more stable atmosphere in these regions based on the model simulations.

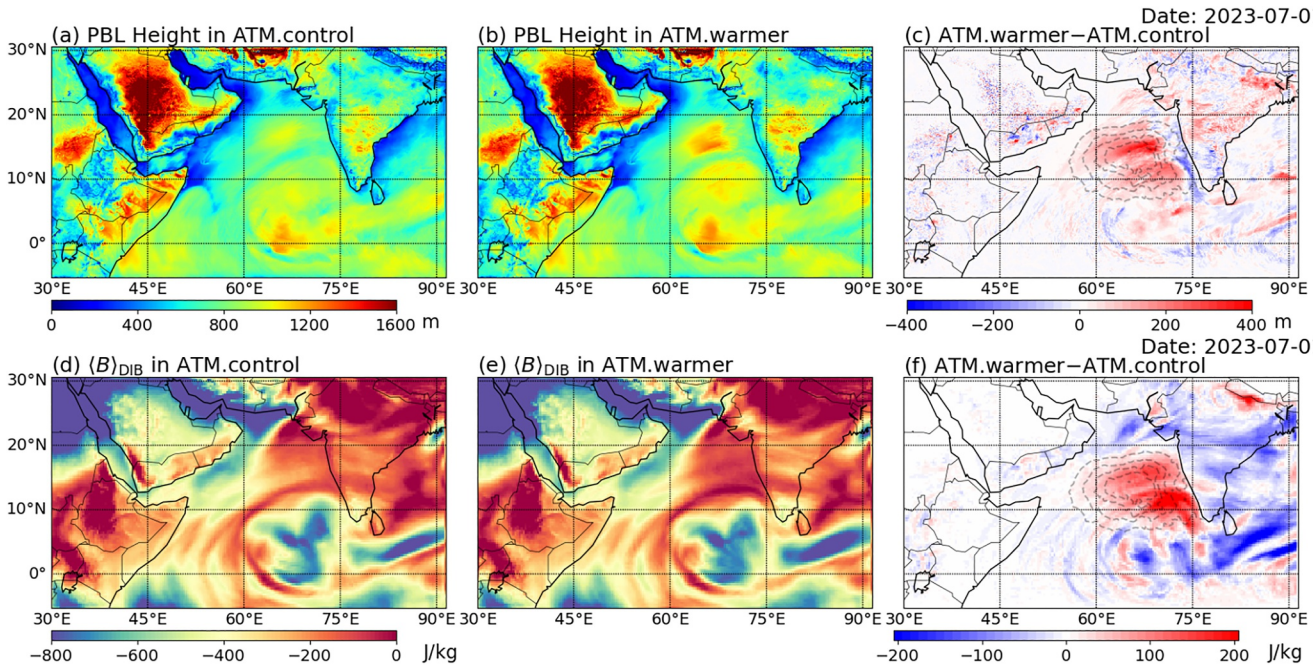

Figure 6. Comparison of PBL height (a, b) and buoyancy $\langle B \rangle_{\mathrm{DIB}}$ (d, e) and their respective differences (c, f) obtained from the experiments. The dashed contours in Panel (c, f) indicate the SST difference shown in Figure 1. The comparisons are shown for 01 July (1 month after the simulation start time).

The vertically integrated buoyancy for 01 July is also shown in Figure 6. The higher values (up to 0 J/kg) indicate an unstable atmosphere; the lower values (down to −800 J/kg) indicate a stable atmosphere. It can be seen that the atmosphere is less stable in the Arabian Sea, but more stable in the Red Sea and the Arabian Gulf. The ATM. warmer case shows higher buoyancy $\langle B \rangle_{\mathrm{DIB}}$ in the warm pool region, indicating that the atmosphere is more unstable and more likely to rain in this region. The buoyancy $\langle B \rangle_{\mathrm{DIB}}$ outside the warm pool decreases, which suggests less likelihood of rainfall. The differences in buoyancy $\langle B \rangle_{\mathrm{DIB}}$ reflect the changes in atmospheric convection that could be because of differences in temperature or humidity between the simulations in and outside of the ASMWP. We will further examine the contributions to different buoyancy fluxes in Section 5.

4. Impacts of SST on IVT

To understand the precipitation differences in the experiments driven by different SST forcing, we examine the variables that contribute to the changes in IVT and IWV. First, we decompose the IVT to compute the contributions of different components to the IVT changes. Then we perform IWV budget analysis to investigate the role of each component in IWV changes. Finally, we examine the vertically integrated buoyancy to show the connections between the changes in atmospheric convection and precipitation.

4.1. Decomposition of IVT

We have shown the IVT difference $\mathrm{IVT}_{\mathrm{diff}}$ in Figure 3c to indicate the difference in water vapor transport between the two experiments driven by different SSTs. To understand the different components contribute to the IVT difference, Figure 7 shows the IVT difference for 01 July decomposed using Equations 9 and 10. The color shading in Panels (b) and (c) indicates the IVT differences contributed from wind speed $\Delta\mathrm{IVT}_{\mathrm{U}}$ and water vapor $\Delta\mathrm{IVT}_{\mathrm{q}}$; the arrows are the vertically integrated $q\Delta\boldsymbol{U}$ and $\boldsymbol{U}\Delta q$. It can be seen that the residual magnitude is smaller than 5 kg/m/s in most of the regions (5% of the max IVT differences), suggesting that the higher-order term and the interpolation error do not play an important role.

Figure 7 shows that the wind contributes to most of the IVT decrease in the northeast Arabian Sea and about 40% of IVT increases (about 40 kg/m/s) between 10 and 15°N in the ASWMP region. The direction of the IVT difference in $q\Delta\boldsymbol{U}$ also agrees with the direction of the total IVT difference in these regions. As discussed in Section 3.2, the difference in wind speed is due to the cyclonic anomalies at lower-level atmosphere generated by

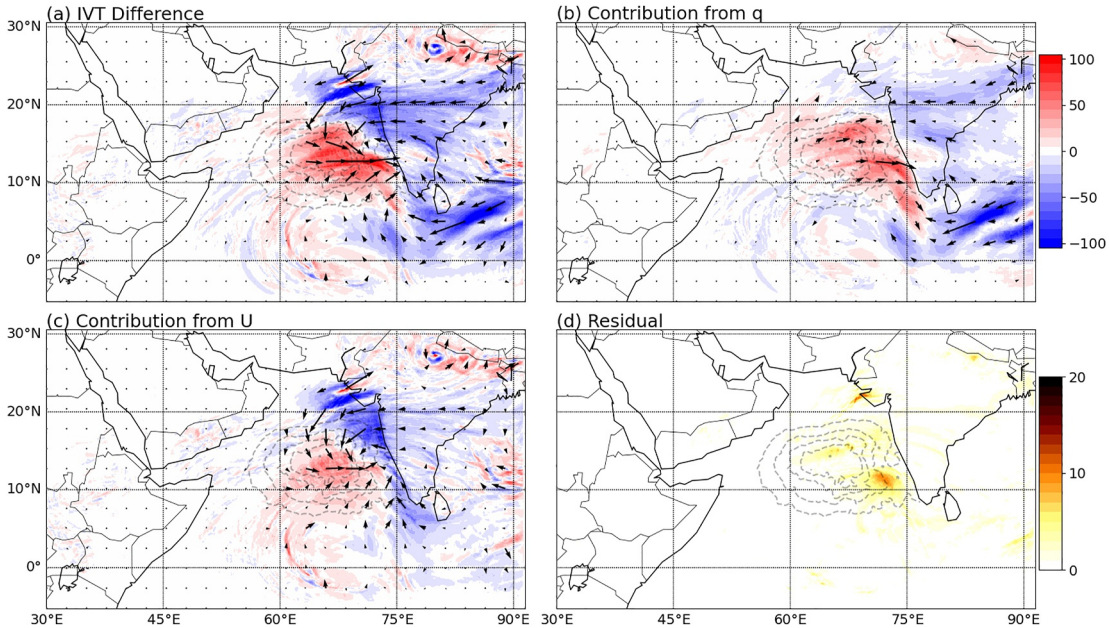

Figure 7. The IVT differences (ATM.warmer−ATM.control) decomposed into different components. Panel (a) is consistent with Figure 3c. The color shading in Panel (b) is IVT differences contributed from water vapor ΔIVT_q; the arrows are the vertically integrated $\boldsymbol{U}\Delta q$. The color shading in Panel (c) is IVT differences contributed from wind speed ΔIVT_U; the arrows are the vertically integrated $q\Delta\boldsymbol{U}$. Panel (d) is the residual including the second-order term and the errors. The residual term is also a vector but for simplicity we only show its magnitude in the plot. The dashed contours in Panel (d) indicate the SST difference shown in Figure 1 at every 0.5°C. The comparisons are shown for 01 July (1 month after the simulation start time).

warmer SST. In addition to the wind, the water vapor plays an important role and contributes to most of the IVT decrease east of 75°E and about 60% of the IVT increases (about 60 kg/m/s) in the warm pool region. The contribution of the water vapor will be further discussed in Section 4.2.

4.2. Water Vapor Budget Analysis

Because the changes in water vapor contribute to most of the IVT decreases east of 75°E and IVT increases in the warm pool region, here we analyze the contribution of the individual terms to understand changes in the water vapor. We first calculate the IWV differences between the two simulations (ATM.warmer−ATM.control) and the differences between each term on the right-hand side of Equation 12, including advection, evaporation, precipitation, and others. Because the budget terms are obtained using the hourly snapshots, all the terms in the budget equation are spatially averaged to a 2.56-degree resolution grid (every 32 grid points in the model) to reduce the uncertainty.

The correlations between the changes in daily IWV and budget terms are shown in Figure 8. Similar to the water vapor budget analysis by Guan et al. (2020), the advection of water vapor plays the dominant role for the monsoon. Except for the warm pool, the correlations range from 0.8 to 1.0 in the western Arabian Sea, south of 10°N, and east of 75°E, showing the importance of water vapor advection. According to Figure 8, the significant water vapor decrease east of 75°E is because of the decrease in incoming water vapor from the ASMWP region. The IVT decrease in Figure 3 also suggests weaker horizontal advection that leads to the decrease in water vapor content east of 75°E. In the ASMWP region between 10° and 20°N, the correlation drops to about 0.4, indicating the importance of changes in other budget terms listed in Equation 12. In the Arabian Sea region, the correlations between the changes in IWV, precipitation, and evaporation are low because these processes have different time scales, especially for the intermittent changes in precipitation shown in Figure 2. In addition, the residual term (not shown) in the budget difference is non-negligible (Guan et al., 2020) due to the relatively small difference between the two simulations. Because of this, it is not easy to analyze the entire contribution of each term in the budget equation. However, it can still be concluded that (a) advection plays an important role in all regions, and (b) the SST changes in ASMWP also impact the water vapor transport by changing the local evaporation and precipitation processes.

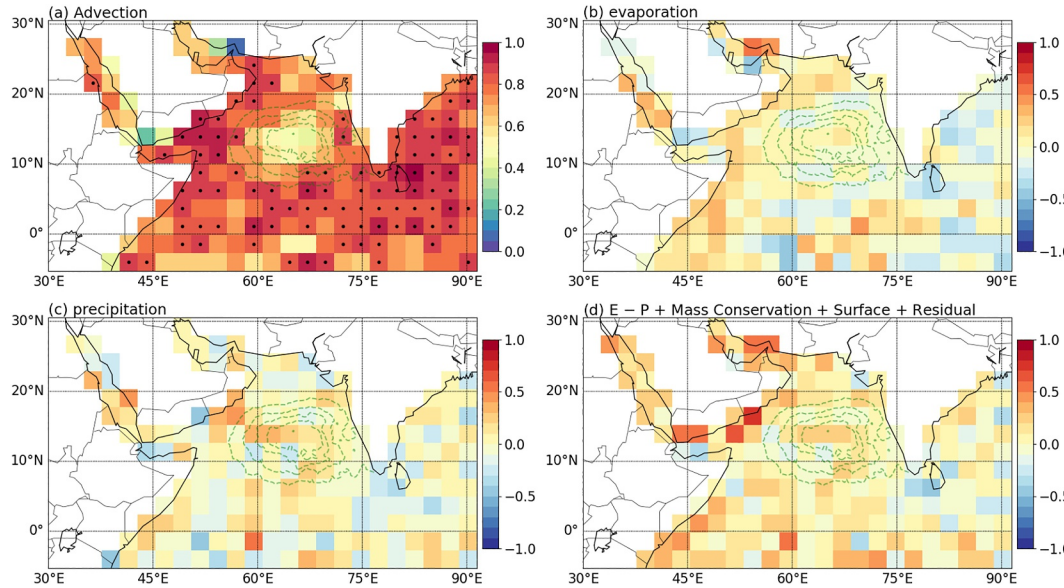

Figure 8. The correlations between the changes in IWV (ATM.warmer−ATM.control) and the budget terms in Equation 12. Panel (a) is the correlation between the IWV and advection changes; Panel (b) is evaporation (E); Panel (c) is precipitation (−P); Panel (d) is the sum of the right-hand side terms except for advection. The contours indicate the SST differences on 01 July to highlight the region of the warm pool. In Panel (a) the regions with correlations larger than 80% are highlighted using black dots. The correlations are computed using the time series of daily IWV and budget terms.

5. Impacts of SST on Vertically Integrated Buoyancy

To further investigate the impact of SST on the precipitation, we examined the changes in vertically integrated buoyancy $\langle B \rangle_{\mathrm{DIB}}$ shown in Figure 6f. Using the equations in Section 2.3, we calculated the $\langle B \rangle_{\mathrm{DIB}}$ using (a) temperature in ATM.control and humidity in ATM.warmer and (b) temperature in ATM.warmer and humidity in ATM.control. This aims to understand the contribution of humidity and temperature to the changes in buoyancy $\langle B \rangle_{\mathrm{DIB}}$. The sensitivity analysis is shown in Figures 9a and 9b for the $\langle B \rangle_{\mathrm{DIB}}$ differences on 01 July. Compared with the $\langle B \rangle_{\mathrm{DIB}}$ differences shown in Figure 6f, most of the changes in buoyancy is due to the differences in humidity, but not directly due to the temperature changes in high SST conditions.

To highlight the buoyancy changes due to humidity or temperature in the WRF experiments, the profiles of virtual temperature are shown in Figures 9c and 9d. The virtual temperature profiles in the WRF models ($T_{v,\mathrm{env}}$) and the plume models ($T_{v,\mathrm{DIB}}$) are plotted at two representative locations (65.84°E, 22.92°N and 65.84°E, 15.24°N), with the areas between the two profiles indicating the vertically integrated buoyancy $\langle B \rangle_{\mathrm{DIB}}$. It can be seen that the environmental virtual temperature $T_{v,\mathrm{env}}$ is warmer for ATM.warmer in the ASMWP (e.g., at 65.84°E, 15.24°N), indicating the atmosphere is unstable; but outside the ASMWP (e.g., at 65.84°E, 22.92°N) $T_{v,\mathrm{env}}$ profiles are almost consistent in two experiments. Figures 9e and 9f show the virtual temperature differences ($T_{v,\mathrm{DIB}} - T_{v,\mathrm{env}}$), with the shading to further examine the impact due to humidity and temperature in the two cases. Outside the ASMWP, the changes in buoyancy $\langle B \rangle_{\mathrm{DIB}}$ are mostly due to the changes in humidity due to horizontal advections as shown in Figure 8a. In the ASMWP region, the temperature contributes to most of buoyancy changes below 850 hPa because increased potential temperature acts to increase the convective instability. On the other hand, the humidity contributes to most of the buoyancy changes between 600 and 800 hPa. Based on the assumption of the idealized plume model, this indicates that a more moist atmosphere could reduce the negative effects of dry air entrainment on the plume buoyancy (Chen et al., 2023; Holloway & Neelin, 2009; Schiro & Neelin, 2019). The significant decrease in $\langle B \rangle_{\mathrm{DIB}}$ east of 75°E and south of 10°N is also due to the water vapor decrease in these regions. As discussed in Section 4.2, the advection of water vapor contributes to 80% of the water vapor changes outside of the ASMWP region, shown in Figure 8a.

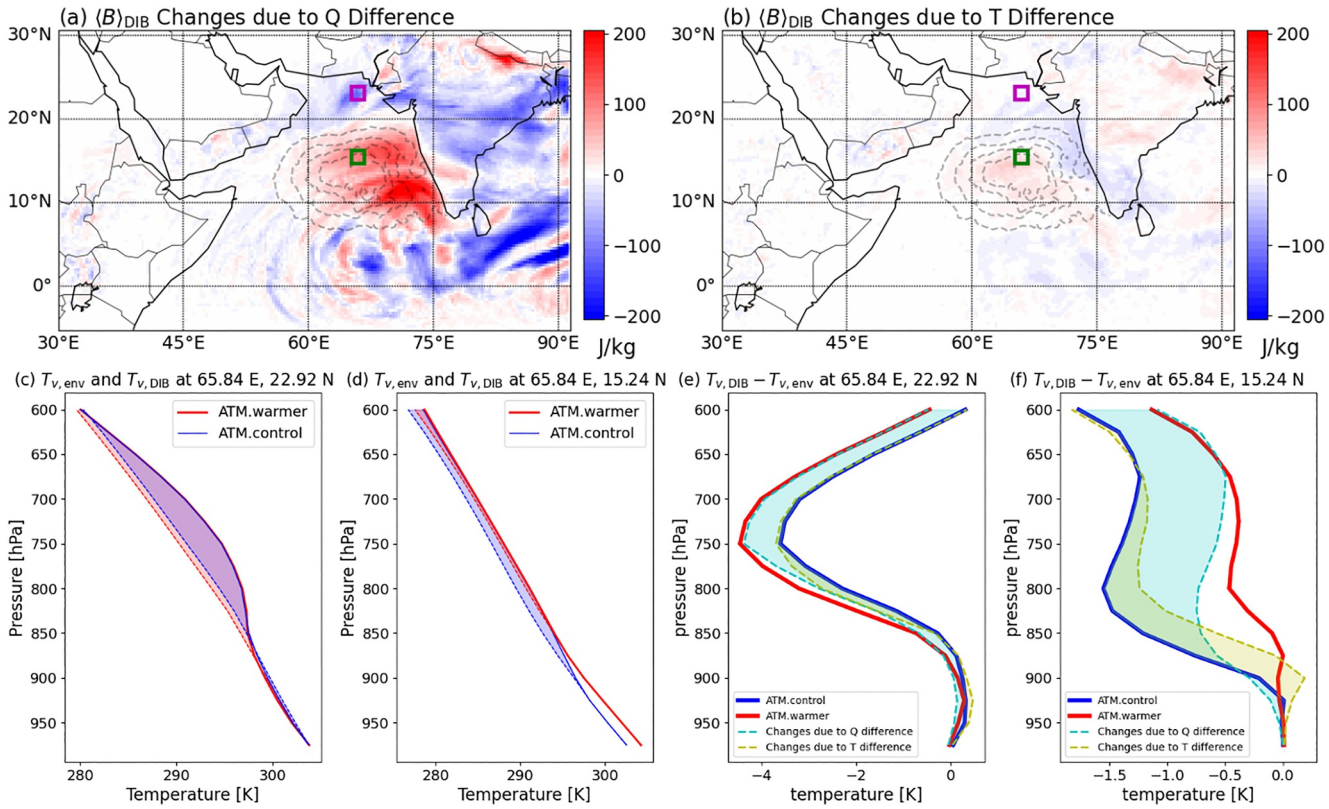

Figure 9. The contribution of humidity and temperature to the differences in vertically integrated buoyancy $\langle B \rangle_{\mathrm{DIB}}$. Panel (a) shows the $\langle B \rangle_{\mathrm{DIB}}$ changes due to humidity differences; Panel (b) shows the $\langle B \rangle_{\mathrm{DIB}}$ changes due to temperature differences. Panel (c, d) are the vertical profiles of virtual temperature $T_{v,\mathrm{DIB}}$ and $T_{v,\mathrm{env}}$ in the WRF model. The shading areas indicate the vertically integrated buoyancy in ATM.warmer (red) and ATM.control (blue). Panel (e, d) show the virtual temperature differences in two cases. The shading areas are the impact of humidity (cyan) and temperature (yellow) on the changes of $\langle B \rangle_{\mathrm{DIB}}$. The virtual temperature profiles are plotted at two representative locations in and outside the ASMWP (magenta box: 65.84°E, 22.92°N; green box: 65.84°E, 15.24°N).

6. Summary and Conclusions

This work investigated the impact of the ASMWP on the north Indian Ocean monsoon. To this end, two WRF simulations were conducted to study the model's sensitivity to SST. OSTIA SST is used in the control run (ATM. control), and was compared with ATM.warmer in which a warmer SST perturbation was added to the warm pool region. In the SST sensitivity experiment, the SST perturbation is about twice the standard deviation of SST from 1981 to 2023. The simulations ran from 01 June to 01 August, aiming to study the monsoon onset and evolution during this period.

Comparing the two simulations, the off-shore precipitation in the warm pool region increased by more than 100%, but outside the warm pool it rained less in the north Arabian Sea and the western coast of India. To understand the differences in precipitation, we examined the water vapor transport during the monsoon in two simulations and found similar increases and decreases in IVT for the same region.

To track the changes in water vapor transport, we decomposed the IVT and found that the changes in water vapor and wind both contribute to the total IVT changes. Based on the water vapor budget analysis, the changes in water vapor are due to (a) stronger evaporation and precipitation in the warm pool region and (b) moisture advection outside the warm pool region. The pressure adjustment mechanism can explain the changes in the wind speed. When the warm pool SST declines more slowly, pressure gradients are generated and cause wind convergence, then the weak cyclonic anomaly of the wind redistributes the water vapor.

In addition, warmer SSTs warm the atmosphere and enhance vertical mixing and convection. To examine the changes in vertical convection, we evaluated the vertically integrated buoyancy from the simulations. The

buoyancy is determined using an idealized plume model from the simulated atmospheric states. We found that when the warm pool cools down more slowly, the buoyancy decreases and the deep convection is more pronounced. The temperature changes contributed to buoyancy changes below 850 hPa within the boundary layer, but the changes in water vapor lead to the most of the differences in buoyancy of the entire atmospheric column.

Future work will involve investigating the air–sea interactions in the warm pool, which can help understand the processes for the generation of the ASMWP and its impact on water vapor transport, especially in the boundary layers. Experiments can be performed to study the air–sea interactions and water vapor transport using the regional coupled modeling system (Sun et al., 2023, 2024) with assimilating in situ observation data collected from the ASTraL/EMAKSAT field campaign. Because this work is inspired by the EMAKSAT field campaign in 2023, an extension of this study is now focusing on year-to-year variability of the ASMWP and its contribution to extreme precipitation events, especially for the southern India region that shows increased precipitation rates with higher SST in ASMWP (Suhas et al., 2026).

Appendix A: Validation of the IVT and Precipitation

The IVT and precipitation obtained in the WRF simulations are validated against ERA5 data and IMERG data, respectively. Figures A1a–A1c show that the IVT obtained in WRF are generally consistent with ERA5 after we applied spectral nudging in the experiments. On the other hand, Figures A1d–A1f show larger discrepancies between the precipitation obtained in the simulations and IMERG. This is because the WRF model has less skill in simulating the precipitations compared with IVT. Because the models has better prediction skill in IVT (Lavers et al., 2016), we studied the IVT differences obtained from the WRF simulations.

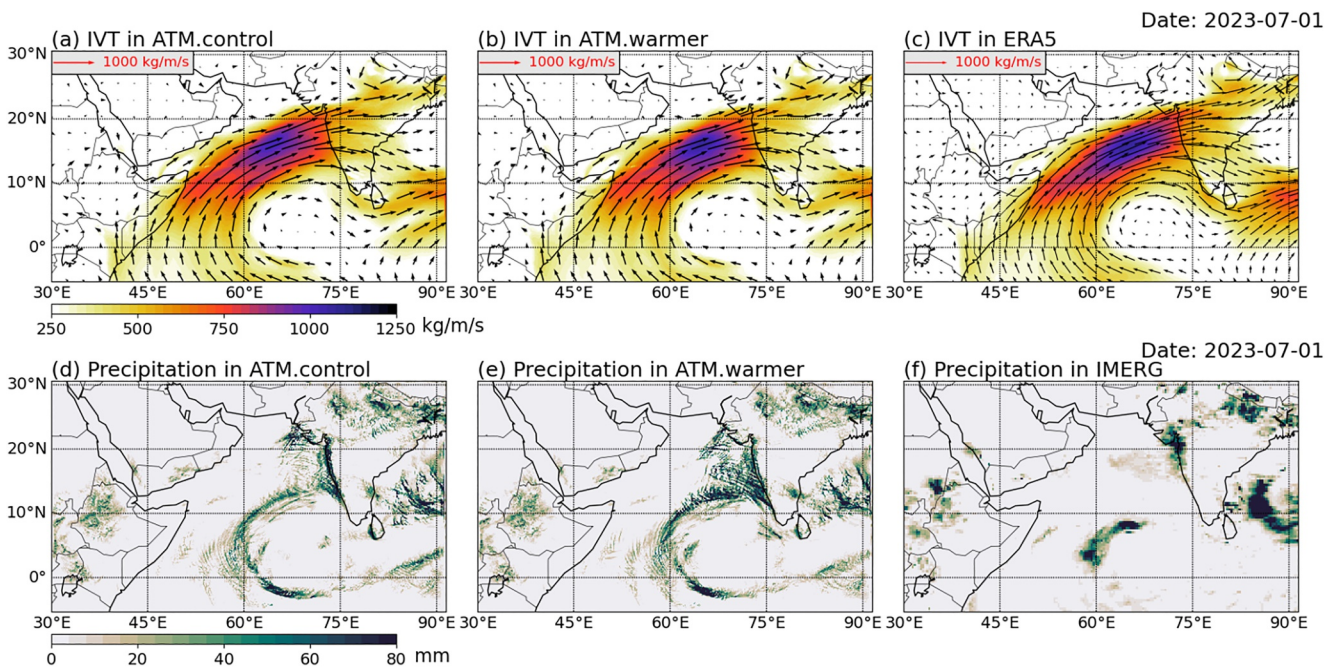

Figure A1. Validation of the IVT and precipitation obtained in the WRF simulations. Panels (a, b) are the IVT contours obtained in ATM.control and ATM.warmer, respectively; Panel (c) is the IVT from ERA5. Panels (d, e) are the precipitations obtained in ATM.control and ATM.warmer, respectively; Panel (f) is the precipitation from IMERG data.

Appendix B: Vertically Integrated Buoyancy

In this work, we use the plume model detailed in Wolding et al. (2024) with the code at https://github.com/bwolding/tropical_PODs. The plume is initiated at the surface and rises and mixes with ambient air according to the prescribed entrainment profile. We use the same "deep-inflow-B" profile (DIB, as in Figure 1 in Wolding et al., 2024), where entrainment occurs over the entire depth of the lower troposphere (Schiro & Neelin, 2019). DIB entrainment corresponds to an idealized sinusoidal convective mass flux profile with a peak at $p_{\text{peak}} = 450$ hPa:

$$m_{\text{mix}}(p) = \sin\left(\frac{\pi}{2}\frac{p_{\text{surface}} - p}{p_{\text{surface}} - p_{\text{peak}}}\right). \tag{B1}$$

A mixing coefficient C_{mix} is calculated at each vertical layer k in the WRF model:

$$C_{\text{mix},k} = \frac{m_{\text{mix}}(p_{k+1}) - m_{\text{mix}}(p_{k-1})}{m_{\text{mix}}(p_{k+1}) + m_{\text{mix}}(p_{k-1})}. \tag{B2}$$

The atmosphere values (i.e., temperature and specific humidity) of the "plume" are then calculated following:

$$r_{\text{plume},k} = (1 - C_{\text{mix},k})\, r_{\text{plume},k-1} + C_{\text{mix},k}\, r_{\text{env},k}, \tag{B3}$$

where $r_{\text{plume},k}$ at surface pressure p_{surface} is the same as the environment r_{env}. We assume that the mixing is local, complete, and instantaneous (Wolding et al., 2024). Ice–liquid water potential temperature is conserved during phase change (Bryan & Fritsch, 2004), and liquid water exceeding 1 g/kg is rained out. The buoyancy is then computed from the vertical profile of the plume virtual temperature $T_{v,\text{plume}}$:

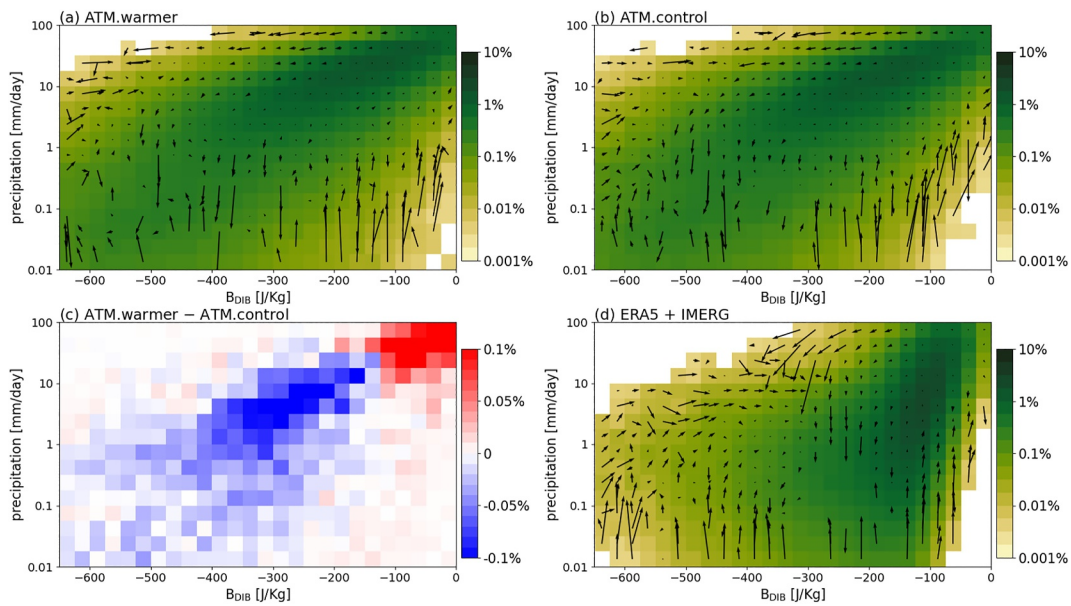

Figure B1. The joint probability density functions of precipitation and vertically integrated buoyancy. Panels (a, b) are the diagrams obtained in ATM.warmer and ATM.control, respectively; Panel (c) is the difference (ATM.warmer−ATM.control); Panel (d) is the diagram obtained by using ERA5 temperature, ERA5 humidity, and IMERG precipitation to validate the simulation results. The shallow convective cycle is between −600 and −350 J/Kg; the deep convective cycle is between −250 and 0 J/Kg. Note the scale of the vector in precipitation is halved to deemphasize the changes. The vectors are indicating the changes in precipitation rate and vertically integrated buoyancy $\langle B \rangle_{\text{DIB}}$ calculated for each a 2-day period (1 day before and 1 day after) following Wolding et al. (2024).

$$\langle B \rangle = \int_{1000\text{hPa}}^{600\text{hPa}} R_d (T_{v,\text{plume}} - T_{v,\text{env}})\, d\ln p, \tag{B4}$$

where R_d is the ideal gas constant; $T_{v,\text{env}}$ is the virtual temperature of the environment. When using the DIB entrainment rate defined in Equation B4, the buoyancy $\langle B \rangle_{\text{DIB}}$ is used to indicate the stability of the atmosphere. It is noted that the surface pressure can be smaller than 1,000 hPa in the WRF model, and thus we compute the $\langle B \rangle_{\text{DIB}}$ from p_{surface} to 600 hPa.

To validate the vertically integrated buoyancy computed from the WRF models, we plot the joint probability density functions (PDFs) of the precipitation and the vertically integrated buoyancy are shown in Figure B1. Because of the mountainous areas on land, the PDFs only use the precipitation and buoyancy in the ocean region. To reduce the uncertainties, we averaged the precipitation and buoyancy to 0.32° resolution (every 4 grid points) used for the precipitation plot in Figure 2. Compared with the validation data in Figure B1d, the WRF simulation results successfully capture the peak of the joint PDF at about −100 J/kg and 10 mm/day, despite some minor differences likely due to the imperfection of WRF in simulating the precipitation. In addition, we plotted the vectors using the bin-averaged differences of both precipitation rate and vertically integrated buoyancy $\langle B \rangle_{\text{DIB}}$. The vectors represent the mean temporal evolution of precipitation and buoyancy over a 2-day period (1 day before and 1 day after) and indicate two regions of cyclical behavior of deep (from −250 to 0 J/kg) and shallow (from −600 to −350 J/kg) convective discharge–recharge cycles (Wolding et al., 2024). In the convective state, the vectors in both cases are pointing upward, showing more precipitation and amplification of convection. The regions between the deep and shallow convective cycles are the transition state. In the transition state, the vectors are both pointing downward, showing less precipitation and decay of convection.

The differences in the PDFs are due to the SST differences in the WRF simulations. In addition, in ATM.warmer SST leads to $\langle B \rangle_{\text{DIB}}$ increases in the deep convection region and $\langle B \rangle_{\text{DIB}}$ decreases in the shallow convection region, shown in Figure B1c. This suggests that the atmosphere is more unstable under warmer SST conditions in the ASMWP region because the buoyancy is more likely to be larger than −100 J/kg, with more evident deep convection under warmer SST conditions. In addition, the PDF is slightly lower in the shallow convection state and there are also fewer arrows pointing upwards in Figure B1a compared with Figure B1b, suggesting the shallow convection cycle is weaker for ATM.warmer case.

Appendix C: Daily Precipitation and IVT at Other Snapshots

The daily precipitation and IVT on 01 July in Section 3 are presented to show their differences. The snapshots on the other days (i.e., 16 June, 16 July, 31 July) are presented in Figures C1 and C2 for precipitation and IVT, respectively. It can be seen in all the snapshots that the IVT increases in the warm pool region and decreases outside of the warm pool. The daily precipitation differences on 16 July and 31 July are associated with the IVT differences: in the warm pool region the off-shore precipitation increases in all three snapshots; in the northern Arabian Sea region and western coast of India between 15 and 20°N the precipitation decreases. It is noted that large discrepancies of precipitation on 16 June is because of the landfall of Cyclone Biparjoy.

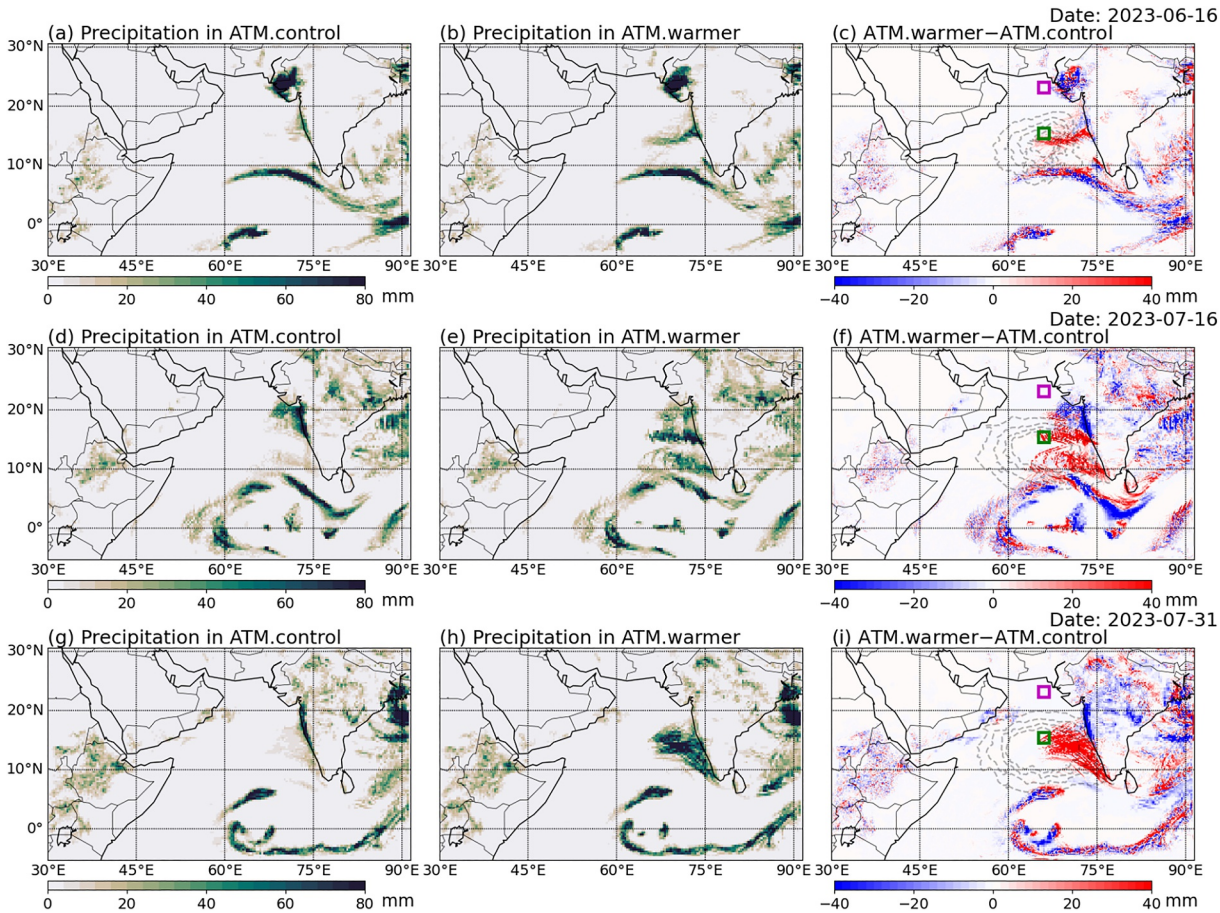

Figure C1. The daily precipitation on 16 June, 16 July and 31 July in the simulations.

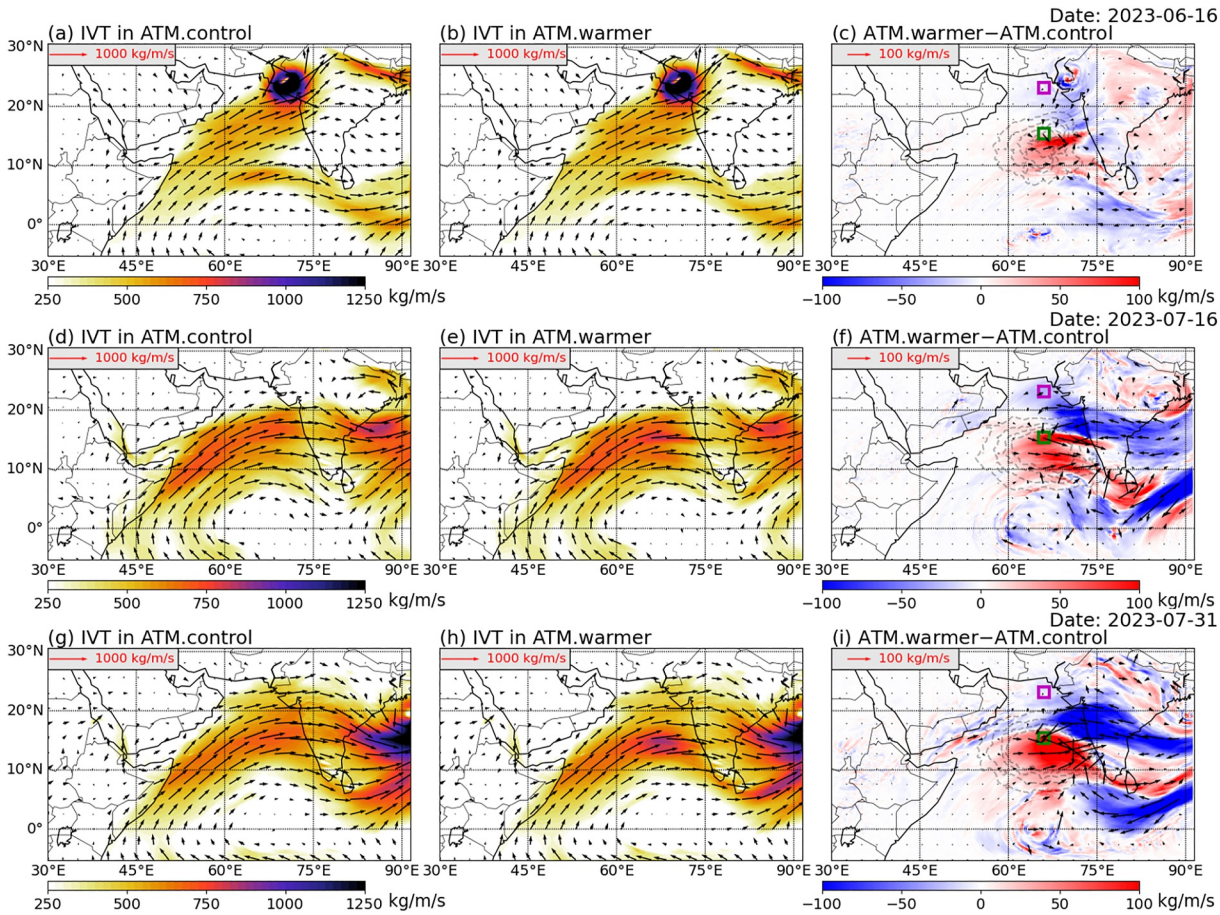

Figure C2. The daily IVT on 16 June, 16 July and 31 July in the simulations.

Appendix D: Horizontal and Vertical Wind Speed

To demonstrate the secondary flow induced by the SST anomalies, the horizontal and vertical wind speed are shown in Figures D1 and D2, respectively. We show the wind speed at three different levels at 925, 700, and 300 hPa. It can be seen in Figure D1 that at 925 hPa the horizontal wind within the boundary layer is generally consistent with the 10-m wind speed shown in Figure 5. This indicates the surface wind redistributes the water vapor within the boundary layer. At 700 hPa, the horizontal wind is weaker than the surface, and the jets from the Arabian Peninsula contribute to the west wind. The differences between ATM.control and ATM.warmer are much smaller at this level. At 300 hPa the easterlies are dominating and strong horizontal wind divergence is observed at this level, which suggests a stronger upward motion of the atmosphere. Figure D2 shows that the vertical wind speed is stronger under warmer SST conditions in the warm pool region. The wind convergence (not shown) computed from the wind speed also suggests increased precipitation in the warm pool region.

The geostrophic wind speed computed from the surface pressure gradient is shown in Figure D3. Because of the small-scale features of the surface pressure, we averaged the surface gradient to a 1.28° resolution grid (every 16 grid points in the model). The geostrophic wind near the equator is not plotted because there is no Coriolis force. Compared with the surface wind speed difference shown in Figure 5c, the magnitude and pattern of the geostrophic wind speed differences are generally consistent, indicating that the pressure adjustment mechanism explains the changes in wind speed. However, we also found significant surface ageostrophic winds that leads to the discrepancies.

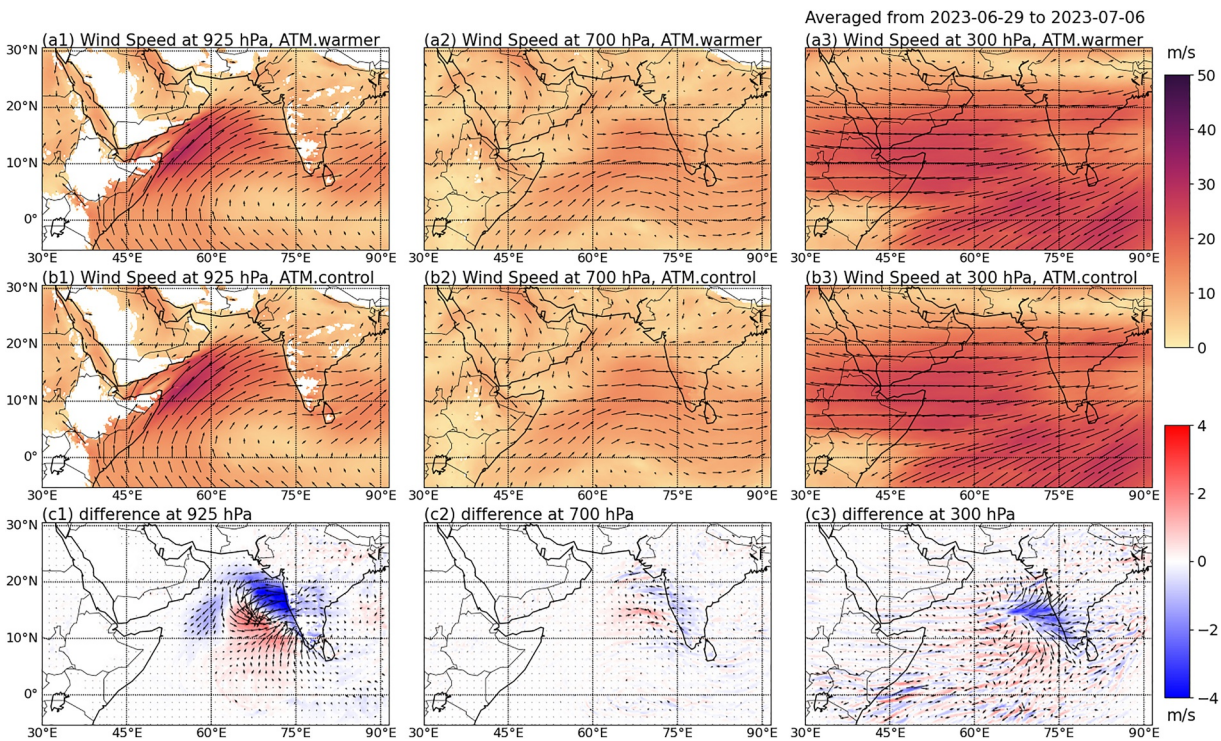

Figure D1. The horizontal wind speed at 925, 700, and 300 hPa. Panels (a, b) show the wind speed obtained from ATM.control and ATM.warmer, respectively. Panel (c) is the difference (ATM.warmer−ATM.control) between the two simulations.

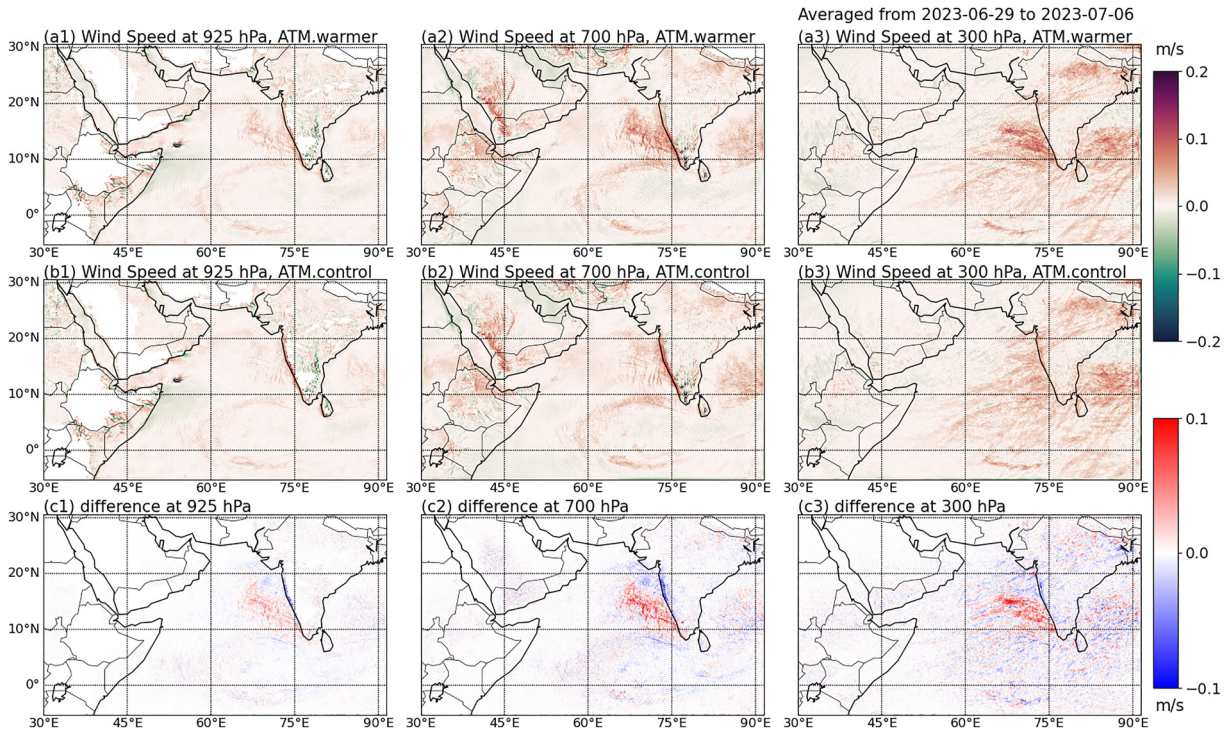

Figure D2. The vertical wind speed at 925, 700, and 300 hPa. Panels (a, b) show the wind speed obtained from ATM.warmer and ATM.warmer, respectively. Panel (c) is the difference (ATM.warmer−ATM.control) between the two simulations.

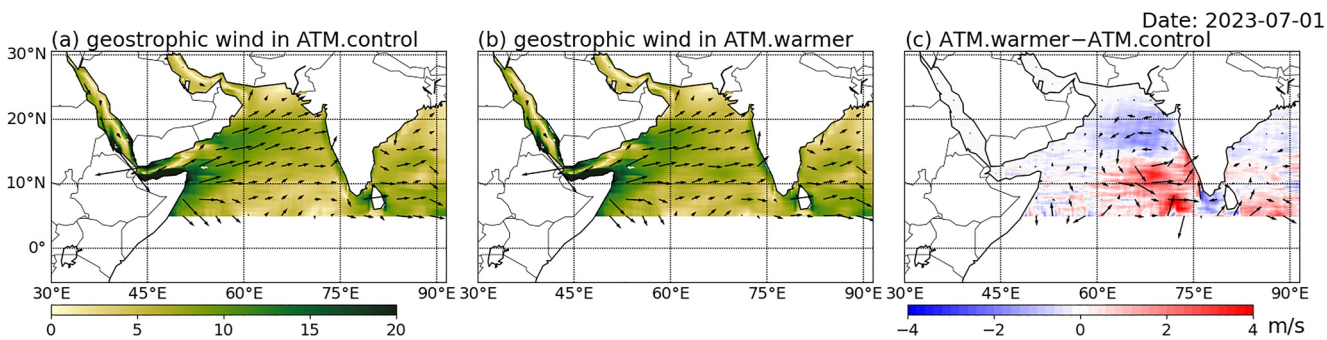

Figure D3. The geostrophic wind speed computed from the surface pressure gradient. Panels (a, b) show the geostrophic wind speed obtained from ATM.control and ATM.warmer, respectively. Panel (c) is the difference (ATM.warmer−ATM.control) between the two simulations.

Conflict of Interest

The authors declare no conflicts of interest relevant to this study.

Availability Statement

The WRF model used for the simulations is described at https://www2.mmm.ucar.edu/wrf/users/download/get_source.html. We obtained the WRF code from https://github.com/wrf-model/WRF/releases/download/v4.5.1/v4.5.1.tar.gz for version 4.5.1. The ERA5 data are obtained from the Copernicus Climate Data Store at https://doi.org/10.24381/cds.adbb2d47 and https://doi.org/10.24381/cds.bd0915c6. The WRF simulation results used in the paper are available at https://doi.org/10.5281/zenodo.15277667.

Acknowledgments
We gratefully appreciate the ONR ASTraL research initiative (N00014-23-1-2092). We also acknowledge the research funding (Grant OSR-2022-NCM-4829.5) from the Climate Change Center at KAUST (King Abdullah University of Science and Technology). ACS was also supported by NOAA Grant NA18OAR4310405 and KAUST CRG Grant ORA-2021-CRG10–4649.2. BW was partially supported by NOAA Cooperative Agreement NA22OAR4320151 and NSF AGS-2225957. BDC and MRM were supported by NOAA Grant NA21OAR4310257, NA18OAR4310403, and NA22OAR4310597. AJM was partly supported by the National Science Foundation (OCE-2022868). JS was supported through the ONR ASTral research Grant N00014-23-1-2091. The simulations were performed on KAUST supercomputer SHAHEEN II and III and we appreciate the computational resources provided by KAUST Supercomputer Laboratory. We thank the comments provided by three anonymous reviewers that substantially improved the manuscript.

References

Back, L. E., & Bretherton, C. S. (2009). On the relationship between SST gradients, boundary layer winds, and convergence over the tropical oceans. *Journal of Climate*, *22*(15), 4182–4196. https://doi.org/10.1175/2009jcli2392.1

Bowden, J. H., Otte, T. L., Nolte, C. G., & Otte, M. J. (2012). Examining interior grid nudging techniques using two-way nesting in the WRF model for regional climate modeling. *Journal of Climate*, *25*(8), 2805–2823. https://doi.org/10.1175/jcli-d-11-00167.1

Bryan, G. H., & Fritsch, J. M. (2004). A reevaluation of ice–liquid water potential temperature. *Monthly Weather Review*, *132*(10), 2421–2431. https://doi.org/10.1175/1520-0493(2004)132<2421:aroiwp>2.0.co;2

Chen, T.-C., & van Loon, H. (1987). Interannual variation of the tropical easterly jet. *Monthly Weather Review*, *115*(8), 1739–1759. https://doi.org/10.1175/1520-0493(1987)115<1739:ivotte>2.0.co;2

Chen, X., Leung, L. R., Feng, Z., & Yang, Q. (2023). Environmental controls on MCS lifetime rainfall over tropical oceans. *Geophysical Research Letters*, *50*(15), e2023GL103267. https://doi.org/10.1029/2023gl103267

Donlon, C. J., Martin, M., Stark, J., Roberts-Jones, J., Fiedler, E., & Wimmer, W. (2012). The operational sea surface temperature and sea ice analysis (OSTIA) system. *Remote Sensing of Environment*, *116*, 140–158. https://doi.org/10.1016/j.rse.2010.10.017

ECMWF. (2017). Era5 data documentation [Dataset] (Tech. Rep.). *European Center for Medium-Range Weather Forecasts*. https://www.ecmwf.int/en/forecasts/dataset/ecmwf-reanalysis-v5

Fita, L., Polcher, J., Giannaros, T. M., Lorenz, T., Milovac, J., Sofiadis, G., et al. (2019). CORDEX-WRF v1. 3: Development of a module for the weather research and forecasting (WRF) model to support the CORDEX community. *Geoscientific Model Development*, *12*(3), 1029–1066. https://doi.org/10.5194/gmd-12-1029-2019

Gadgil, S. (2003). The Indian monsoon and its variability. *Annual Review of Earth and Planetary Sciences*, *31*(1), 429–467. https://doi.org/10.1146/annurev.earth.31.100901.141251

Gimeno-Sotelo, L., & Gimeno, L. (2023). Where does the link between atmospheric moisture transport and extreme precipitation matter? *Weather and Climate Extremes*, *39*, 100536. https://doi.org/10.1016/j.wace.2022.100536

Glisan, J. M., Gutowski, W. J., Jr., Cassano, J. J., & Higgins, M. E. (2013). Effects of spectral nudging in WRF on arctic temperature and precipitation simulations. *Journal of Climate*, *26*(12), 3985–3999. https://doi.org/10.1175/jcli-d-12-00318.1

Guan, B., Waliser, D. E., & Ralph, F. M. (2020). A multimodel evaluation of the water vapor budget in atmospheric Rivers. *Annals of the New York Academy of Sciences*, *1472*(1), 139–154. https://doi.org/10.1111/nyas.14368

Hersbach, H., Bell, B., Berrisford, P., Biavati, G., Horányi, A., Muñoz Sabater, J., et al. (2023). ERA5 hourly data on pressure levels from 1940 to present [Dataset] (Tech. Rep.). *ERA5 hourly data on single levels from 1940 to present. Copernicus Climate Change Service (C3S) Climate Data Store (CDS)*. https://doi.org/10.24381/cds.bd0915c6

Hersbach, H., Bell, B., Berrisford, P., Biavati, G., Horányi, A., Muñoz Sabater, J., et al. (2023). ERA5 hourly data on single levels from 1940 to present [Dataset] (Tech. Rep.). *Copernicus Climate Change Service (C3S) Climate Data Store (CDS)*. https://doi.org/10.24381/cds.adbb2d47

Holloway, C. E., & Neelin, J. D. (2009). Moisture vertical structure, column water vapor, and tropical deep convection. *Journal of the Atmospheric Sciences*, *66*(6), 1665–1683. https://doi.org/10.1175/2008jas2806.1

Huang, B., Liu, C., Banzon, V., Freeman, E., Graham, G., Hankins, B., et al. (2021). Improvements of the daily optimum interpolation sea surface temperature (DOISST) version 2.1. *Journal of Climate*, *34*(8), 2923–2939. https://doi.org/10.1175/jcli-d-20-0166.1

Iacono, M. J., Delamere, J. S., Mlawer, E. J., Shephard, M. W., Clough, S. A., & Collins, W. D. (2008). Radiative forcing by long-lived greenhouse gases: Calculations with the AER radiative transfer models. *Journal of Geophysical Research*, *113*(D13). https://doi.org/10.1029/2008jd009944

Kain, J. S. (2004). The Kain–Fritsch convective parameterization: An update. *Journal of Applied Meteorology*, *43*(1), 170–181. https://doi.org/10.1175/1520-0450(2004)043<0170:tkcpau>2.0.co;2

Kingsmill, D. E., & Houze, R. A., Jr. (1999). Thermodynamic characteristics of air flowing into and out of precipitating convection over the west Pacific warm pool. *Quarterly Journal of the Royal Meteorological Society*, *125*(556), 1209–1229. https://doi.org/10.1002/qj.1999.49712555606

Kuo, Y.-H., & Neelin, J. D. (2022). Conditions for convective deep inflow. *Geophysical Research Letters*, *49*(20), e2022GL100552. https://doi.org/10.1029/2022gl100552

Kurian, J., & Vinayachandran, P. (2007). Mechanisms of formation of the Arabian Sea mini warm pool in a high-resolution ocean general circulation model. *Journal of Geophysical Research*, *112*(C5). https://doi.org/10.1029/2006jc003631

Lakshmi, D. D., Satyanarayana, A., & Chakraborty, A. (2019). Assessment of heavy precipitation events associated with floods due to strong moisture transport during summer monsoon over India. *Journal of Atmospheric and Solar-Terrestrial Physics*, *189*, 123–140. https://doi.org/10.1016/j.jastp.2019.04.013

Lavers, D. A., Waliser, D. E., Ralph, F. M., & Dettinger, M. D. (2016). Predictability of horizontal water vapor transport relative to precipitation: Enhancing situational awareness for forecasting Western US extreme precipitation and flooding. *Geophysical Research Letters*, *43*(5), 2275–2282. https://doi.org/10.1002/2016gl067765

Li, N., Zhu, X., Wang, H., Zhang, S., & Wang, X. (2023). Intraseasonal and interannual variability of sea temperature in the Arabian Sea warm pool. *Ocean Science*, *19*(5), 1437–1451. https://doi.org/10.5194/os-19-1437-2023

Li, Y., & Carbone, R. (2012). Excitation of rainfall over the tropical Western Pacific. *Journal of the Atmospheric Sciences*, *69*(10), 2983–2994. https://doi.org/10.1175/jas-d-11-0245.1

Lindzen, R. S., & Nigam, S. (1987). On the role of sea surface temperature gradients in forcing low-level winds and convergence in the tropics. *Journal of the Atmospheric Sciences*, *44*(17), 2418–2436. https://doi.org/10.1175/1520-0469(1987)044<2418:otross>2.0.co;2

McGee, C. J., & van den Heever, S. C. (2014). Latent heating and mixing due to entrainment in tropical deep convection. *Journal of the Atmospheric Sciences*, *71*(2), 816–832. https://doi.org/10.1175/jas-d-13-0140.1

Meehl, G. A. (1994). Influence of the land surface in the Asian summer monsoon: External conditions versus internal feedbacks. *Journal of Climate*, *7*(7), 1033–1049. https://doi.org/10.1175/1520-0442(1994)007<1033:iotlsi>2.0.co;2

Morrison, H., Thompson, G., & Tatarskii, V. (2009). Impact of cloud microphysics on the development of trailing stratiform precipitation in a simulated squall line: Comparison of one-and two-moment schemes. *Monthly Weather Review*, *137*(3), 991–1007. https://doi.org/10.1175/2008mwr2556.1

Nagamani, P., Ali, M., Goni, G., Udaya Bhaskar, T., McCreary, J., Weller, R., et al. (2016). Heat content of the Arabian Sea mini warm pool is increasing. *Atmospheric Science Letters*, *17*(1), 39–42. https://doi.org/10.1002/asl.596

Nakanishi, M., & Niino, H. (2004). An improved Mellor–Yamada level-3 model with condensation physics: Its design and verification. *Boundary-Layer Meteorology*, *112*(1), 1–31. https://doi.org/10.1023/b:boun.0000020164.04146.98

Nakanishi, M., & Niino, H. (2009). Development of an improved turbulence closure model for the atmospheric boundary layer. *Journal of the Meteorological Society of Japan. Series II*, *87*(5), 895–912. https://doi.org/10.2151/jmsj.87.895

Neema, C., Hareeshkumar, P., & Babu, C. (2012). Characteristics of Arabian Sea mini warm pool and Indian summer monsoon. *Climate Dynamics*, *38*(9–10), 2073–2087. https://doi.org/10.1007/s00382-011-1166-2

Radu, R., Déqué, M., & Somot, S. (2008). Spectral nudging in a spectral regional climate model. *Tellus A: Dynamic Meteorology and Oceanography*, *60*(5), 898–910. https://doi.org/10.1111/j.1600-0870.2008.00341.x

Raghuvanshi, A. S., & Agarwal, A. (2023). Unraveling atmospheric moisture transport linkages to extreme precipitation events and associated synoptic features over India. *Journal of Hydrology*, *626*, 130290. https://doi.org/10.1016/j.jhydrol.2023.130290

Ralph, F. M., Dettinger, M. D., Cairns, M. M., Galarneau, T. J., & Eylander, J. (2018). Defining "atmospheric river": How the glossary of meteorology helped resolve a debate. *Bulletin of the American Meteorological Society*, *99*(4), 837–839. https://doi.org/10.1175/bams-d-17-0157.1

Ralph, F. M., Rutz, J. J., Cordeira, J. M., Dettinger, M., Anderson, M., Reynolds, D., et al. (2019). A scale to characterize the strength and impacts of atmospheric rivers. *Bulletin of the American Meteorological Society*, *100*(2), 269–289. https://doi.org/10.1175/bams-d-18-0023.1

Rao, R., & Sivakumar, R. (1999). On the possible mechanisms of the evolution of a mini-warm pool during the pre-summer monsoon season and the genesis of onset vortex in the South-Eastern Arabian Sea. *Quarterly Journal of the Royal Meteorological Society*, *125*(555), 787–809. https://doi.org/10.1256/smsqj.55502

Reynolds, R. W., Smith, T. M., Liu, C., Chelton, D. B., Casey, K. S., & Schlax, M. G. (2007). Daily high-resolution-blended analyses for sea surface temperature. *Journal of Climate*, *20*(22), 5473–5496. https://doi.org/10.1175/2007jcli1824.1

Roman-Stork, H. L., Subrahmanyam, B., & Murty, V. (2020). The role of salinity in the southeastern Arabian Sea in determining monsoon onset and strength. *Journal of Geophysical Research: Oceans*, *125*(1), e2019JC015592. https://doi.org/10.1029/2019jc015592

Roxy, M., Gnanaseelan, C., Parekh, A., Chowdary, J. S., Singh, S., Modi, A., et al. (2020). *Indian Ocean warming. Assessment of climate change over the Indian region: A report of the ministry of Earth sciences (MoES)* (pp. 191–206). Government of India.

Saikrishna, T., Ramu, D. A., Prasad, K. H., Osuri, K., & Rao, A. (2022). High resolution dynamical downscaling of global products using spectral nudging for improved simulation of Indian monsoon rainfall. *Atmospheric Research*, *280*, 106452. https://doi.org/10.1016/j.atmosres.2022.106452

Schiro, K. A., Ahmed, F., Giangrande, S. E., & Neelin, J. D. (2018). GoAmazon2014/5 campaign points to deep-inflow approach to deep convection across scales. *Proceedings of the National Academy of Sciences*, *115*(18), 4577–4582. https://doi.org/10.1073/pnas.1719842115

Schiro, K. A., & Neelin, J. D. (2019). Deep convective organization, moisture vertical structure, and convective transition using deep-inflow mixing. *Journal of the Atmospheric Sciences*, *76*(4), 965–987. https://doi.org/10.1175/jas-d-18-0122.1

Seager, R., & Henderson, N. (2013). Diagnostic computation of moisture budgets in the ERA-interim reanalysis with reference to analysis of CMIP-archived atmospheric model data. *Journal of Climate*, *26*(20), 7876–7901. https://doi.org/10.1175/jcli-d-13-00018.1

Shenoi, S., Shankar, D., & Shetye, S. (1999). On the sea surface temperature high in the Lakshadweep Sea before the onset of the southwest monsoon. *Journal of Geophysical Research*, *104*(C7), 15703–15712. https://doi.org/10.1029/1998jc900080

Skamarock, W. C., Klemp, J. B., Dudhia, J., Gill, D. O., Liu, Z., Berner, J., et al. (2019). A description of the advanced research WRF model version 4 [Software]. (Tech. Rep. No. 10.5065), *145*. https://www2.mmm.ucar.edu/wrf/users/docs/technote/v4_technote.pdf

Suhas, D. L., Han, W., Shinoda, T., Sun, R., Subramanian, A., Bourassa, M., & Alexander, M. (2026). Marine heatwaves in the Arabian Sea: Drivers and impacts on atmospheric circulation and extreme precipitation. arXiv preprint arXiv:2603.18319.

Sun, R., Cobb, A., Villas Bôas, A. B., Langodan, S., Subramanian, A. C., Mazloff, M. R., et al. (2023). Waves in SKRIPS: WAVEWATCH III coupling implementation and a case study of tropical cyclone Mekunu. *Geoscientific Model Development*, *16*(12), 3435–3458. https://doi.org/10.5194/gmd-16-3435-2023

Sun, R., Sanikommu, S., Subramanian, A. C., Mazloff, M. R., Cornuelle, B. D., Gopalakrishnan, G., et al. (2024). Enhanced regional ocean ensemble data assimilation through atmospheric coupling in the SKRIPS model. *Ocean Modelling*, *191*, 102424. https://doi.org/10.1016/j.ocemod.2024.102424

Sun, R., Subramanian, A. C., Cornuelle, B. D., Mazloff, M. R., Miller, A. J., Ralph, F. M., et al. (2021). The role of air–sea interactions in atmospheric rivers: Case studies using the SKRIPS regional coupled model. *Journal of Geophysical Research: Atmospheres*, *126*(6), e2020JD032885. https://doi.org/10.1029/2020jd032885

Tang, J., Wang, S., Niu, X., Hui, P., Zong, P., & Wang, X. (2017). Impact of spectral nudging on regional climate simulation over CORDEX East Asia using WRF. *Climate Dynamics*, *48*(7), 2339–2357. https://doi.org/10.1007/s00382-016-3208-2

Tewari, M., Chen, F., Wang, W., Dudhia, J., LeMone, M., Mitchell, K., et al. (2004). Implementation and verification of the unified NOAH land surface model in the WRF model. In *20th Conference on weather analysis and forecasting/16th conference on numerical weather prediction* (Vol. 1115).

Vinayachandran, P., Kurian, J., & Neema, C. (2007). Indian Ocean response to anomalous conditions in 2006. *Geophysical Research Letters*, *34*(15). https://doi.org/10.1029/2007gl030194

Washington, W. M., Chervin, R. M., & Rao, G. (1977). Effects of a variety of Indian Ocean surface temperature anomaly patterns on the summer monsoon circulation: Experiments with the NCAR general circulation model. *Pure and Applied Geophysics*, *115*(5–6), 1335–1356. https://doi.org/10.1007/bf00874412

Weisse, R., Heyen, H., & Von Storch, H. (2000). Sensitivity of a regional atmospheric model to a sea state–dependent roughness and the need for ensemble calculations. *Monthly Weather Review*, *128*(10), 3631–3642. https://doi.org/10.1175/1520-0493(2000)128<3631:soaram>2.0.co;2

Wolding, B., Rydbeck, A., Dias, J., Ahmed, F., Gehne, M., Kiladis, G., et al. (2024). Atmosphere–ocean coupled energy budgets of tropical convective discharge–recharge cycles. *Journal of the Atmospheric Sciences*, *81*(1), 3–29. https://doi.org/10.1175/jas-d-23-0061.1